AN ABSTRACT OF THE THESIS OF

Job Michael Guidos for the degree of Master of Science in Physics presented on April 12, 2022.

Title: SpaceLab, an N-Body Particle-Particle Ballistic Collision Simulation Tool with Applications in Celestial Body Dynamics

Abstract approved: _____

Davide Lazzati

This thesis conveys the key technical features and scientific applications of a particle-particle ballistic simulation tool (SpaceLab) as well as a high level overview of experiments it was designed for and executed on. SpaceLab simulates spherical particle interactions under any combination of self-gravity, sliding friction, rolling friction, Van-Der-Waals (VDW) cohesion force, elastic repulsion, and restitution. SpaceLab particle interactions are never instantaneous and ensure sufficient interaction time between particles to conserve energy not lost to restitution to within 1% per collision. SpaceLab has been used to explore both the gravity dominated and VDW dominated scales, including hundreds of kilometer rubble-pile asteroids and micron sized dust grains comprised of up to 10,000 particles with desired material properties, size variation, and control over a wide range of initial conditions. High velocity projectiles are also facilitated with dynamic time-stepping to accurately simulate sce-

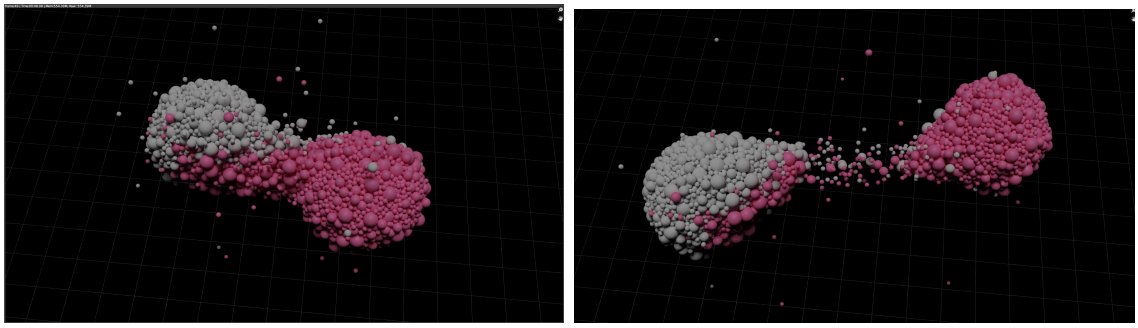

Figure 1: Two rubble-piles in a glancing collision. One cluster colored all pink begins on the left, and the other all white begins on the right. After a glancing collision of two rubble-piles, an exchange of particles occurs. Mostly intact, the two rubble-piles drift apart. Please see https://sss.aeromap.org/animations for full animation.

narios like the DART mission[2]. Conglomerate objects and both scales are tested for resilience to collisions with various sized projectiles, speeds, and spins to define constraints for collision remnant growth. The data gained from these experiments may be used to determine what conditions facilitate the growth of asteroids into planets, or dust grains into larger objects significantly effected by gravity. We also verify that the tool's results agree with similar work in literature and attribute key differences to features we include that are still uncommon in the field, such as the inclusion of surface friction which we find to increase collision remnant bound mass due to increase dissipation of collision energy. Future development plans for performance improvement and user friendly interface are also briefly discussed. Figure 1 shows a typical off-center collision of two clusters of particles which may be used to model rubble-pile asteroid collisions. These figures demonstrate a common scenario simulated with SpaceLab.

Various animated results can be found at https://sss.aeromap.org/animations

SpaceLab, an N-Body Particle-Particle Ballistic Collision Simulation Tool with Applications in Celestial Body Dynamics

by

Job Michael Guidos

A THESIS

submitted to

Oregon State University

in partial fulfillment of
the requirements for the
degree of

Master of Science

Presented April 12, 2022
Commencement June 2022

Master of Science thesis of Job Michael Guidos presented on April 12, 2022.

APPROVED:

Major Professor, representing Physics

Head of the Department of Physics

Dean of the Graduate School

I understand that my thesis will become part of the permanent collection of Oregon State University libraries. My signature below authorizes release of my thesis to any reader upon request.

Job Michael Guidos, Author

ACKNOWLEDGEMENTS

We acknowledge support from NASA grants 80NSSC18K1729. Perhaps unconventionally, I would like to acknowledge Wikipedia, The Free Encyclopedia as a priceless learning resource and springboard for numerous investigations. I believe Wikipedia deserves far more respect and acknowledgement than it gets. It is a marvel of human cooperation and contribution. I, Job Guidos, acknowledge Dr. Davide Lazzati for outstanding influence in my academic career and beyond. Without this project and a very healthy working relationship, I would not be where I am. He took the initiative to suggest the fitting grant for this work after I had been away from university for two years. He also did the brunt of the work to secure the grant. I owe my current employment in my dream job in large part to the progression of this project and all I have learned from him.

TABLE OF CONTENTS

TABLE OF CONTENTS (Continued)

LIST OF FIGURES

LIST OF FIGURES (Continued)

LIST OF FIGURES (Continued)

Figure Page

LIST OF TABLES

LIST OF APPENDIX FIGURES

Chapter 1: Introduction

It is taken for granted that planets are formed from the protoplanetary disc of their host stars, but key areas still require investigation, including the formation of small grains from the disc, their growth into asteroids, and the conditions under which asteroids form into planetesimals. The work of SpaceLab seeks to facilitate investigations like these.

This paper will attempt to cover two scales of application. The kilometer scale rubble-pile asteroid at nearly 500km in diameter, as well as the micron scale in which dust grains are formed from particles 2 tenths of a micron in diameter. Each scale will be addressed where necessary. In cases where there is no difference in treatment, only one may be addressed.

There is a quickly growing interest in asteroid exploration for various purposes including potential resource extraction and planetary defense. These include mission like DART[2], OSIRIS-REx[3], Hayabusa2[6], and several others, many of which are listed at NASA's website[1].

In one example usage of SpaceLab, simulation of the impact of the DART probe with the surface of Didymos b (the moonlet of the asteroid pair in the DART mission) is carried out using the detailed mission specifications such as probe dimensions, mass, and impact velocity, as well as current estimates of the mass and density of the moonlet. See Figures 5.1 and 5.2.

Other challenges such as landing safely on a rubble-pile are apparent in the Philae probe getting stuck in a crack after attempting to land on comet 67p. Simulations that can better predict the structure and stability of rubble-piles may contribute to more successful sample collision and perhaps eventually harvesting asteroids.

Similar investigations have been carried out by Leinhardt, Et al.[7], and Sanchez, Et al.[11]. Our results are compared with those while noting the significance of surface friction, rolling resistance, varied particle size, and realistic material properties not all present in either case.

1.1 Objective

The objective of this work is to help raise the standard for physically accurate ballistic particle collisions in astrophysics simulations which often omit some or all of the following: Surface friction, cohesion, rolling resistance, varied particle radii, and restitution. These features have often been omitted with good reason, typically due to hardware and time constraints, as adding such features significantly impacts computation time and memory usage. In spite of this, we set out to put physical accuracy first, pay the price in simulation time and hardware limitations later, and in the future, improve performance with advanced methods such as tree structures, GPU parallelism, and state based dynamic time resolution.

1.2 Background

This work is a continuation of my undergraduate thesis. The project began with the straight forward goal presented by Dr. Davide Lazzati to model billiard ball collisions which included an interaction duration sufficient to model friction and elastic repulsion. Gravity and restitution were quickly added while verifying conservation of energy not attributed to restitution. After writing some code to generate a "cluster" of particles that could be collided with another cluster, it became immediately apparent that this could be a good model for asteroid collisions, among other things. From there the tool features and set of simulations continued to grow.

Chapter 2: Materials and Reasoning

2.1 "Cluster" Clarification

In this work the terms cluster, rubble-pile, conglomerate, or grain may be used interchangeably to mean a bunch of particles stuck together by either their own gravitational force or VDW force.

2.2 Programming Languages

Python was used to developed the original concept. Later, the project was converted to C++ for improved performance control and because of the wide demand for C++ competence in industry. Python continues to be used for post-simulation analysis and visualization via the Blender Python API. In testing, an order of magnitude decrease in computation times was observed by switching from Python to C++. Expert users of Python will rightly tell you that you can get comparable performance from Python when using carefully chosen modules and avoiding native Python loops and conditionals. Numpy is a prime example of a powerful and fast Python module written in C. Numpy is well accepted and integrated, but it only gets more complex from there to achieve what C++ has natively. That effort was instead spent learning C++.

2.3 Data Visualization

2.3.1 Blender

Initially, the VPython package for Python was used to visualize particle systems in 3D, but Blender with its Python API was later chosen for more powerful visualization control such as scrubbing back and forth in the animation, rendering, and built in measuring tools, as well as better performance.

Figure 2.1 shows the best of the VPython visualizations. Figures 2.2 and 2.3 show a rendered 3D simulation result using the Blender Python API as well as a convenient control interface for viewing the results and creating presentation.

The value of a good visualization in 3D simulation work cannot be overstated. Too often, an incredible amount of work in scientific simulation will go into creating accurate results, only to be squandered on poor visualization that is hard to interpret and doesn't read well. There is certainly something to be said for the most simple representation of data, but my suggestion is that a little extra effort to use lighting, shadows, and textures (especially for spinning objects) goes a long way in making inspiring visual representation. Perhaps more importantly, it makes for "readable" 3D representations, leading to better understanding and intuition building for phenomena still only able to be simulated on a computer screen, such as asteroid collisions. Such visuals should not always be used in place of data plots, but most often in combination with them.

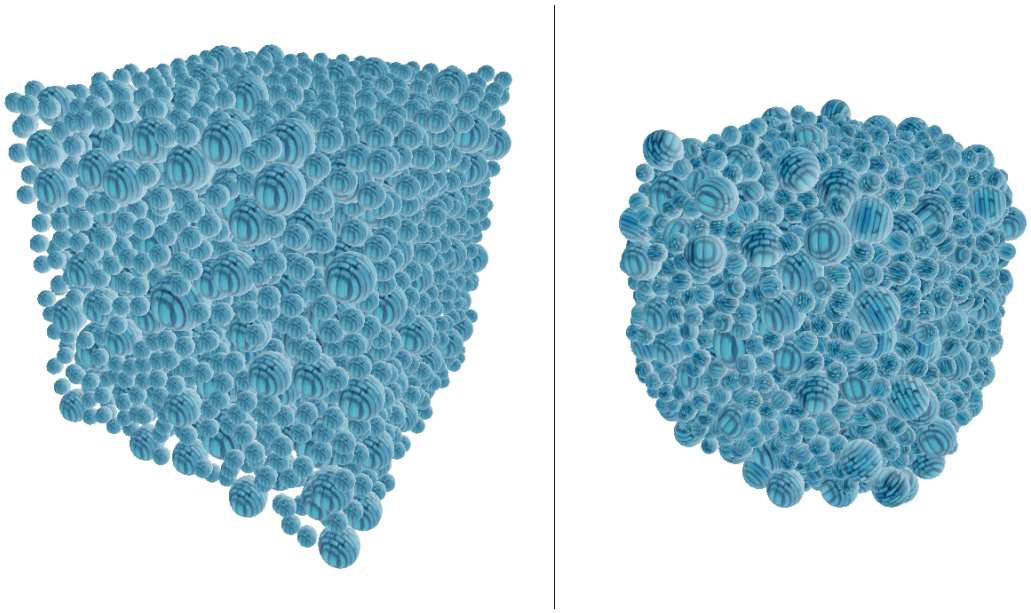

Figure 2.1: Old cluster formation method with cubic distribution.

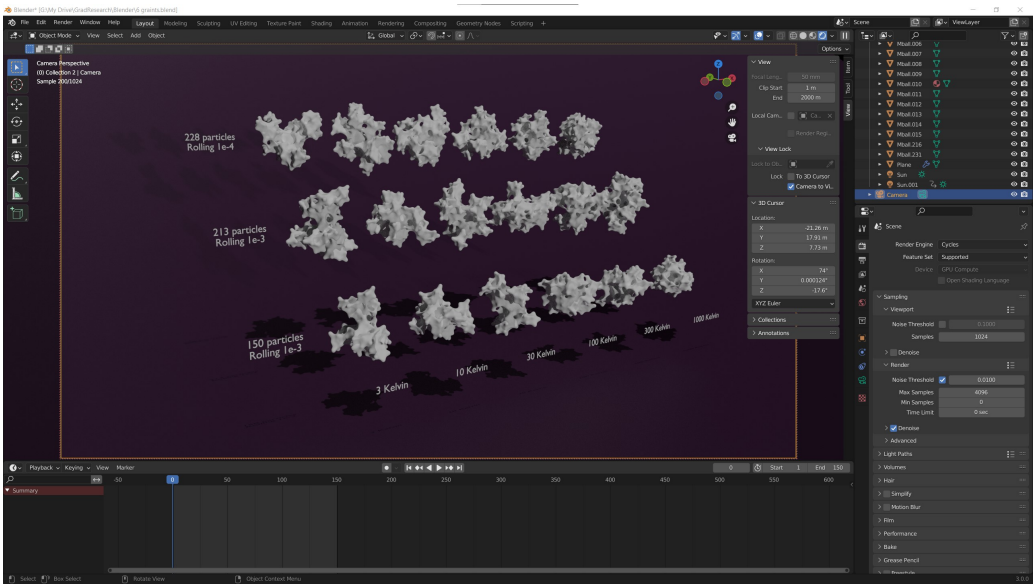

Figure 2.2: Dust creation results in Blender

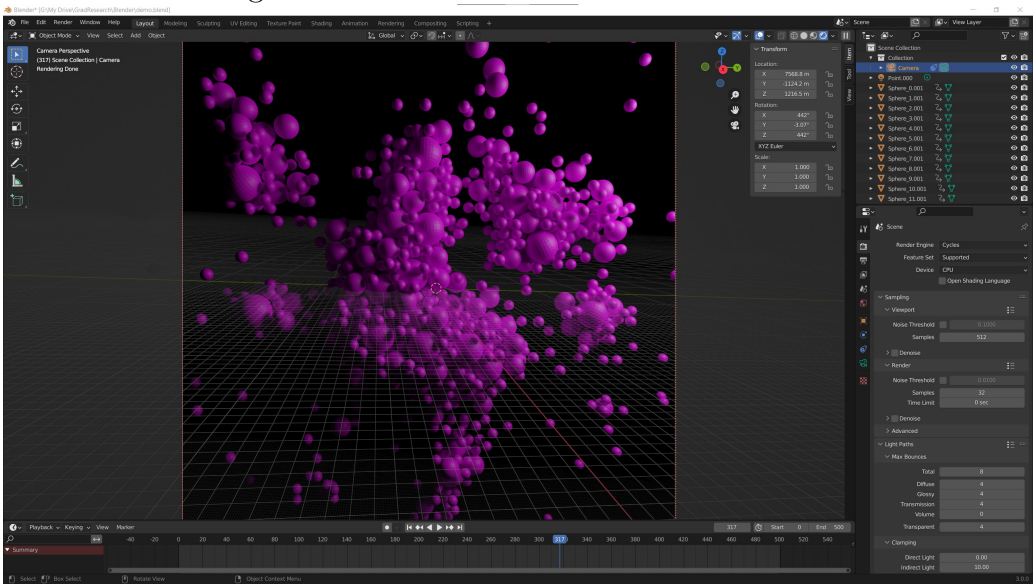

Figure 2.3: Asteroid spin-up in Blender

Chapter 3: Methods

3.1 Discrete Element Method

The discrete element method (DEM)[14] is chosen due to the desire to model the fine detail of individual particle interactions both in contact (friction, elastic, etc) and at range (gravity or VDW). Continuum approaches, though generally faster, are limited both in long distance interactions as well as tracking discrete particle interaction. The most notable disadvantage of DEM is that it is relatively computationally intensive. The current implementation has the worst case time complexity of $\mathcal{O}(n^2)$ such that every particle interacts with every other particle in the system on every time-step. Interactions between particles only occur in all combinations, not all permutations, meaning that if particle A has interacted with particle B, particle B interacts with particle A in the same iteration, so the number of iterations is not n^2, but $\frac{n}{2}(n+1)$. Optimizations such as a Barnes-Hut Tree [10] are currently in development but not fully integrated. This will improve time complexity to as little as $\mathcal{O}(n \cdot log(n))$.

3.2 Integration Method

The half-step velocity Verlay method [15] is chosen for all simulations thus far. Several methods of integration were considered. Velocity Verlet, Runge-Kutta (RK4), and Richardson Extrapolation. The Verlet method yielded an optimal combination

of computational speed and accuracy. The half-step velocity Verley method is shown in Eqs. (3.1)-(3.4).

$$x(i+1) = x(i) + v(i)\delta t + \frac{1}{2}a(i)\delta t^2 \tag{3.1}$$

$$v\left(i+\frac{1}{2}\right) = v(i) + \frac{1}{2}a(i)\delta t \tag{3.2}$$

$$a(i+1) = \text{Acceleration due to gravity using current position} \tag{3.3}$$

$$v(i+1) = v\left(i+\frac{1}{2}\right) + \frac{1}{2}a(i+1)\delta t \tag{3.4}$$

where x is displacement, $v(i+\frac{1}{2})$ is the velocity "half-step", a is acceleration, and finally $v(i+1)$ is the completed velocity computation for the current time-step. The same algorithm is used to compute angular quantities for particle rotation.

3.3 Catastrophic Disruption Threshold

$Q*$ represents the energy at which the mass of the largest remnant is equal to half of the total mass of both clusters. In this work mass of the largest remnant, M_{lr}, divided by total mass are indicated explicitly, and energy of collision is represented as $\eta = \frac{T}{U}$ where T is the total kinetic energy at the point of collision, and U is the total potential energy among both clusters.

$$\frac{M_{lr}}{M_{tot}} = -0.5(\frac{QR}{Q^*_{RD}} - 1) + 0.5 \tag{3.5}$$

This quantity is converted in our work to compare results with Leinhardt Et al. 2012[7]. The original definition is found in Leinhardt Et al. 2011[8].

3.4 Elastic Repulsion

A "soft collision" in which a collision interaction occurs over multiple time-steps is necessary for the implementation of surface friction. For this reason, the particles are treated as compressing springs. The harmonic oscillator, Eq. (3.6), is the chosen model for repulsion,

$$\vec{F_s} = -k\frac{R_i + R_j - ||\vec{r}_{ij}||}{j}\hat{r} \tag{3.6}$$

where $||\vec{r}_{ij}||$ is the distance between particles i and j, R_i and R_j are the respective radii of particles i and j, and the factor $\frac{R_i+R_j-||\vec{r}_{ij}||}{j}$ determines the compression experienced by particle i from particle j. When particles are colliding, this additional surface normal force is added to the gravitational force for the current time-step to simulate the collision 'bounce'.

3.5 Restitution

Kinetic energy is removed from particles in collision by directly altering the elasticity constant, k. During particle collision, if in the current time-step, the particles have become farther apart than they were in the previous time-step, the elasticity constant is changed to αk where α is a value less than 1. $\alpha = 0.8$ is chosen as a reasonable coefficient for general "rocky" material representation[5]. The resulting weaker re-

pulsion during exit from collision effectively removes energy from the system. This method provides a velocity independent coefficient of restitution of $\sqrt{\mu_k}$.

A dashpot method such as the one implemented in Sanchez Et al. [11] was also considered and tested. Using the dashpot method did not provide any significant advantage over the course of our simulations, and does not allow for constant coefficient of restitution across all scales. Figures 4.6, 4.7, and 4.8 show the result of both methods.

3.6 Sliding Friction

To determine sliding friction, two primary physical quantities must be derived. These are the relative surface velocity experienced by particle i of particle j, and the normal force, $\vec{N}$, exerted during collision. The normal force of collision is the elastic repulsion force, $\vec{F}_{elastic}$. The relative surface velocity that particle i experiences on particle j depends on both particles' angular velocity, as well as the component of their linear velocity tangent to their surfaces at the point of collision.

3.6.0.1 Derivation

The vector from the center of particle i to the point of contact on the surface is found by Eq. (3.7).

$$\vec{r}_{i,contact} = \frac{R_i}{R_i + R_j}\vec{r}_{ij} \tag{3.7}$$

Where R is the radius of a particle and $\vec{r}_{ij}$ is the vector from the center of particle i to the center of particle j. This vector represents the lever arm used to apply force and torque from particle j onto particle i.

The surface velocity of particle i at the point of contact is found as:

$$\vec{v}_{i,surface} = \underbrace{\vec{v}_i - (\vec{v}_i \cdot \vec{r}_{ij})\frac{\vec{r}_{ij}}{||\vec{r}_{ij}||}}_{\text{velocity component tangent to surface}} + \underbrace{\vec{\omega}_i \times \frac{R_i}{R_i + R_j}\vec{r}_{ij}}_{\text{velocity due to rotation}} \tag{3.8}$$

Where $\vec{\omega_i}$ is angular velocity of particle i. The relative surface velocity is then the difference between the surface velocities of the two particles:

$$\vec{v}_{i,surface,relative} = \vec{v}_{j,surface} - \vec{v}_{i,surface} \tag{3.9}$$

The friction force experienced by particle i is therefore

$$\vec{F}_{i,friction} = -\mu_k ||\vec{F}_{elastic}|| \hat{v}_{i,surface,relative} \tag{3.10}$$

where μ_k is the coefficient of friction.

The torque on particle i is then:

$$\frac{2}{5} m_i R_i^2 \frac{d\omega_i}{dt} = \frac{R_i}{R_i + R_j}\vec{r}_{ij} \times \vec{F}_{i,friction} \tag{3.11}$$

The friction force is equal and opposite for particle j, so the necessary information to move both interacting particles is known from a single calculation. By dividing the torque by the respective moment of inertia, the angular acceleration applied due

to surface friction is found.

3.7 Gravitational Force

In the gravity dominated regime of asteroids, gravity is applied between all particles in the standard discrete force based approach:

$$\vec{F}_g = G\frac{m_i m_j}{r^2}\hat{r}_{ij} \tag{3.12}$$

3.8 Van-Der-Waals Force (VDW)

VDW force is applied in place of gravity for dust-scale attraction and cohesion. The model used for VDW force, Tayeb Et al. 2015[13], calculation is

$$\vec{F}_{vdw} = \frac{Ha}{6}\frac{64R_i^3R_j^3(h+R_i+R_j)}{(h^2+2R_ih+2R_j)^2(h^2+2R_ih+2R_jh+4R_iR_j)^2} \tag{3.13}$$

An h_{min} is also enforced which overrides h when two particles are nearly touching

Ha	Hamaker Constant
R_i	Radius i
R_j	Radius j
h	Distance to nearest contact

to prevent stability issues due to exponential scaling. This technically makes the cohesive force between particles artificially low and will be considered in our ongoing research in dust resilience to collisions.

3.9 Rolling Resistance (Rolling Friction)

Rolling resistance, also known as, rolling friction, is the phenomenon by which objects rolling along each other's surface slow down. This phenomenon is critical to the microscopic regime, Santos Et al. 2020, [12] of dust grain formation. For example, if particles i and j are in contact under VDW force and another particle k adheres to j, if their is no rolling resistance, it will roll along the surface of j until it encounters i. This results in highly compact structures. Material constants for rolling resistance remain quite elusive in literature, so part of the ongoing investigation in this work is to determine how significant the coefficient of rolling friction is to the formation of dust grains. The model used for rolling resistance is as follows. Let us call $\vec{F}_{sf}$ the force of sliding friction. The rolling friction produces a force on particle i:

$$\vec{F}_{rf} = -\mu_{fr}\|\vec{F}_n\|\frac{(\vec{\omega}_i - \vec{\omega}_j) \times \vec{r}_i}{\|(\vec{\omega}_i - \vec{\omega}_j) \times \vec{r}_i\|} \tag{3.14}$$

The net friction force would then be:

$$\vec{F}_{nf} = \vec{F}_{sf} + \vec{F}_{rf} \tag{3.15}$$

and the torque applied to particle i:

$$\vec{\tau}_i = \vec{r}_i \times \vec{F}_{nf} \tag{3.16}$$

3.10 Simulation Stability and Error

3.10.1 Elasticity, Time-step, and Velocity, a Dynamic Balance

A large challenge addressed in SpaceLab is accurately simulating very hard, rocky particles as springs with a multi-time-step collision duration. Such objects in other works are most often simulated using instantaneous collisions due to the tiny time step size necessary to resolve a non-zero interaction time with low error in conserved quantities. We instead ensure that all particles have a minimum interaction time sufficient to conserve energy with an error less than 1%. This puts energy error during collision at least an order of magnitude lower than the loss of energy due to intentional restitution. This numerical accuracy is consider acceptable. It is also important for the elasticity constant to be high enough to reasonably represent rock.

In order for the code to remain stable and conserve energy, a sufficiently large elasticity constant and a sufficiently small time-step need to be carefully chosen. The requirements are as follows:

1. The maximum compression, Δx, anywhere in the simulation needs to be a small fraction, dR, of the radius of the colliding particles. A maximum compression of $0.1R$ is chosen for all scenarios discussed in this paper.

2. At each time-step, dt, the displacement of the fastest particle must only be a small fraction of the maximum compression, such that sufficient time-steps are taken during the collision. For two particles i and j colliding with velocity v_i and v_j in their centers of mass, the compression can be written as:

$$\Delta x_{ij} = \frac{1}{2}\frac{m_i v_i^2}{k}\left(1 + \frac{m_i}{m_j}\right) \tag{3.17}$$

In order to ensure stability (i.e., that particles cannot penetrate each-other) we require:

$$\Delta x_{ij} \ll \frac{r_i + r_j}{2} \tag{3.18}$$

Rearranging the terms and using $m_i = 4\pi/3\,\rho r_i^3$ we obtain:

$$k \gg 2\frac{\frac{4\pi}{3}\rho r_i^3 v_i^2\left(1 + \frac{m_i}{m_j}\right)}{r_i^2\left(1 + \frac{r_j}{r_i}\right)^2} \tag{3.19}$$

If we assume that i is the lighter particle, then $\left(1 + \frac{m_i}{m_j}\right) \leq 2$ and $\left(1 + \frac{r_j}{r_i}\right) \geq 2$ and we conclude that the condition on the elasticity constant is:

$$k \gg \frac{4\pi}{3}\rho r_{\max} v_{\max}^2 \tag{3.20}$$

where $r_{\max}$ is the radius of the biggest particle in the simulation and $v_{\max}$ is the speed of the fastest particle in the simulation. In most cases, the above condition yields a minimum constant for physical reliability that is much smaller than the actual Young's modulus of rocks, which is of the order of 10^{10} barye, Malkowski Et al. 2020[9].

The condition on the time-step is inextricably linked to the chosen elasticity constant. A larger constant yields more stiff particles and therefore smaller compression,

which requires a smaller time-step to compensate. The condition we enforce is

$$v_{\max} dt \ll \Delta x_{ij} \tag{3.21}$$

which, after analogous calculations, yields

$$dt \ll \sqrt{\frac{m_{\min}}{k}} \tag{3.22}$$

where $m_{\min}$ is the mass of the smallest particle in the simulation.

It is to be noted that the actual value of the elasticity constant adopted only affects the duration of a particle-particle bounce, but not its outcome, nor the forces involved. It is not necessary to use the actual elasticity of the material in order to obtain reasonable outcomes. For that reason, it is more productive to select a value that satisfies Eq.(3.20) and then use Eq.(3.22) to derive the required time-step.

3.11 Bound Cluster Identification

A post-simulation code was developed in Python to identify stable, bound remnant particle clusters. First an adaptive Gaussian smoothing filter is run with a local standard deviation equal to ten times the particle radius across all particles. Then, the highest point in the filtered distribution is identified and used as the first guess for a suitable bound cluster based on density of particle distribution. A second pass iterates through all particles and determines if each particle is energetically bound to the guess cluster. Nearest particles are analyzed first to ensure that the mass of the

whole cluster is included when the membership of a distant particle is investigated. After the first cluster and all its member particles are identified, they are removed from the set. The Gaussian filter is run again, and the process is repeated to identify the second cluster. This cycle is repeated until all particles have been accounted for in a bound remnant, or the number of desired remnant identifications is reached. Figure 4.13 shows a rubble-pile collision with particles colored by their eventual bound clusters. The goal is to show where, throughout the rubble-pile, the particles in a remnant come from. Figure 4.14 shows how the 5 largest remnants distribute and begin to recombine.

3.12 Data Format

Several data output and storage approaches are considered including some standard database types, and CSV. A CSV format was found time and again to be the best choice because of the convenience of data inspection. However, with future work planned to improve performance with tree structures, the OpenVDB format is being considered as it natively stores data in a tree structure and has proven performance benefits in the field of visual effect simulation. For now, the data is organized into three files: simData, constants, and energy. The simData file contains one row per recorded time-step, with groups of 11 elements per particles including three for position, three for velocity, four for angular velocity (including magnitude directly computed). The constants file includes particle mass, radius, and moment of inertia. The energy file includes kinetic and potential energy, momentum, angular momen-

tum, and total energy of the system per time-step. Though some of these quantities can be derived directly from others, this is the set found most convenient for data visualization, animation, and direct data inspection.

3.13 Material Properties and Cluster Composition

3.13.1 Rubble-Pile Asteroid

Table 3.1 provides a sample parameter set for a 34KM rubble-pile. The particle density, $2.65 g/cm^3$, was chosen as a reasonable approximation for the composition of asteroids[4]. Coefficient of friction of 0.3 was chosen based on rough approximations and assumptions of asteroid composition and rocky material observations. A key point is that this value is on the low end of potential friction coefficient so as not to over-represent the effect of friction in our experiments, as friction is somewhat of a novel inclusion as mentioned previously.

Particle size was determined within three constraints; computation time, attempting to maintain constant rubble-pile mass, and a distribution of mass between three particle radii to ensure that no significant lattice structure forms. Surface friction implemented in these simulations also impedes the formation of lattice structures. The radii used for the three particle sizes varies with particle count to maintain rubble-pile mass and volume. The forces in play are not scale free from mass and volume. Rubble-pile mass is split evenly, by mass, between the three particle sizes, therefore, the formula for calculating the number of particles of each size is Eqs. (3.23), (3.24), and (3.25). Particle size was then automatically adjusted dependent

on the number of particles in a rubble-pile formation, by Eq. (3.26).

$$\text{Large particle count} = particles * 1/31.375 \tag{3.23}$$

$$\text{Medium particle count} = particles * 27/(8 * 31.375) \tag{3.24}$$

$$\text{Small particle count} = particles * 27/31.375 \tag{3.25}$$

$$\text{Scaling Factor} = \frac{10^3}{3 * particles} \tag{3.26}$$

3.13.2 Calculating Rubble-Pile Density

Estimating the average rubble-pile density was especially important when simulating the DART mission because we had estimates of the specific moonlet mass and diameter. To estimate density, the cluster was assumed to be a perfect sphere, and the distance of the farthest particle from its center of mass was taken as its radius. In this way the cluster porosity is accounted for. Table 3.1 shows comparison of the particle density with cluster density.

3.14 Cluster Formation Methods

3.14.1 Rubble-Pile Asteroid Formation

A stable particle cluster represents a rubble-pile asteroid. Particles are first uniformly distributed in a plausible spherical space based on hexagonal close packing. A collision check is run across all particle pairs and if a collision is detected, one particle is moved randomly to another location in the sphere. This process is repeated with a tolerance of 200 tries for all particles. If any collisions are detected after 200 tries, the sphere radius is increased by $2 \times R_{max}$, the radius of the largest particle in the system and all particle positions are re-randomly distributed and the process starts again. This eventually leads to a reasonably well packed random set of particles, saving time in the next step. The loosely packed particles are then allowed to collapse under their own gravity into a more compact and stable structure. A rubble-pile formation is considered complete when the kinetic energy of the system is constant and by visual inspection of the collapse in Blender, Figure 3.4. Material and composition parameters can be found in Table 3.1. A set of simulation runs for an asteroid with progressively more granular particle resolution can be found in Table 3.3.

In early implementations of cluster formation, the random distribution of particles filled a cube instead of a sphere. Because we compute friction, this resulted in cube-like clusters. We took advantage of this to determine if "edge-to-edge", "corner-to-corner", and "face-to-face" collisions had significantly different results. Figure 3.1 shows an example of the cube-like collision configuration.

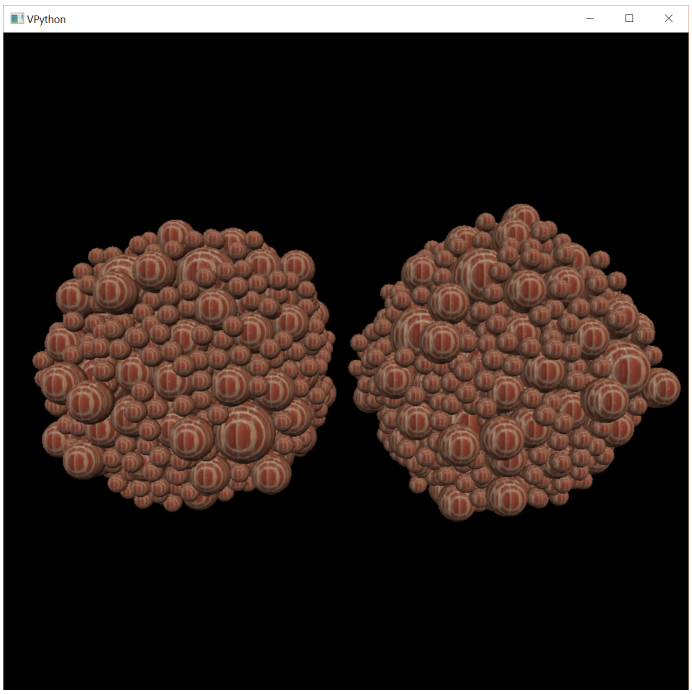

Figure 3.1: Two cube-like clusters configured to collide such that the left cluster is face first and the right cluster is edge first in the collision. The purpose of this test is to determine how sensitive the collision outcome is to deviations from more spherical cluster shape.

Table 3.1: Simulation constants for rubble-pile asteroid formation ($\tilde{3}$4km diameter)

Simulation duration	t	=	12000 *seconds*
Time-step duration	dt	=	0.4 *seconds*
Elasticity constant	k	=	10^15 $dyne/cm$
Gravitational constant	G	=	6.67×10^{-8} $dyne \cdot cm^2/g^2$
Coefficient of friction	μ	=	0.3
Coefficient of restitution	e	=	0.9
Particle density	ρ	=	2.65 g/cm^3
Particle radius	R	=	See Section 3.13 and Table 3.3
Rubble-pile mass	$M_\oplus$	$\approx$	$2.9 \pm 0.2 \times 10^{10}$ g
Rubble-pile radius	$R_\oplus$	=	1780 ± 130 or 90000 ± 5000 cm
Rubble-pile density	$\rho_\oplus$	$\approx$	2.41 g/cm^3
Rubble-pile separation	D	=	3300 or 3700 cm

Table 3.2: Additional Rubble-Pile Formation Definitions

Total kinetic energy	T	erg
Total potential energy	U	erg
Mass of largest remnant	M_{lr}	g
Mass of target	M_t	g
Mass of projectile	M_t	g
Normalized specific impact energy	Q/Q^*_D	
Q to disperse half target mass[1]	Q^*_D	erg/g

Table 3.3: Rubble-pile Formation Sample

Particles	Radii (cm) $[Count]$			Friction	Seeds[2]
10	1392 [0]	928 [1]	464 [9]	Yes	1
20	1105 [1]	737 [2]	368 [17]	Yes	1
40	877 [1]	585 [4]	292 [35]	Yes	1
60	766 [2]	511 [6]	255 [52]	Yes	1
80	696 [3]	464 [9]	232 [68]	Yes	2
100	646 [3]	431 [11]	215 [86]	Yes	1
120	608 [4]	405 [13]	203 [103]	Yes	1
160	553 [5]	368 [17]	184 [138]	Yes	2
200	513 [6]	342 [22]	171 [172]	Yes	1
300	300 [10]	200 [32]	100 [258]	No	1
320	439 [10]	292 [34]	146 [276]	Yes	2
400	407 [13]	271 [43]	136 [344]	Yes	1
500	378 [16]	252 [54]	126 [430]	Yes	1
640	348 [20]	232 [69]	116 [551]	Yes	2
1000	300 [32]	200 [108]	100 [860]	No	1
1000	300 [32]	200 [108]	100 [860]	Yes	1
1280	276 [41]	184 [138]	92 [1101]	Yes	10
1280	126 [1280]	All	same	Yes	1
2560	219 [82]	146 [275]	73 [2203]	Yes	1
5120	174 [163]	116 [551]	58 [4406]	Yes	1

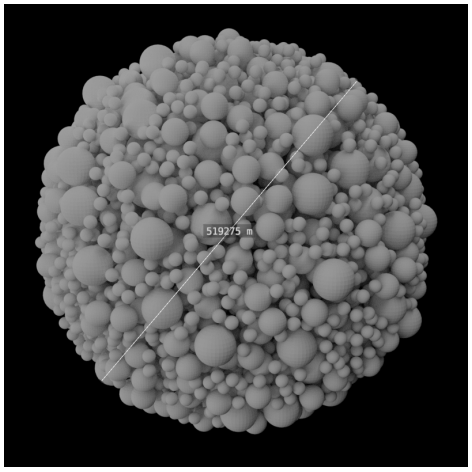

Figure 3.2: Before collapse

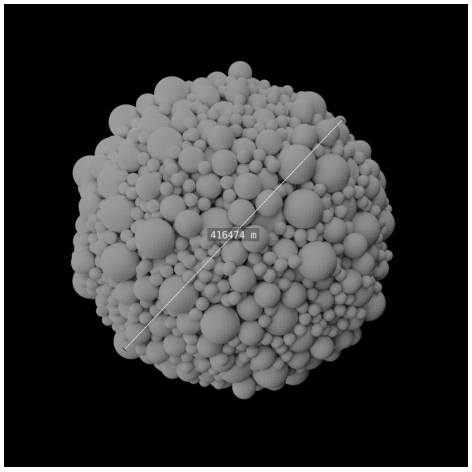

Figure 3.3: After collapse

Figure 3.4: A spherical cluster is formed by tightly randomly distributing particles in a sphere volume while ensuring no contact between particles. A simulation is then run allowing the particles to collapse by their own gravity and settle into a stable rubble-pile. Note the change in diameter after collapse. This is one challenge in producing an asteroid with specific diameter, density, and mass.

3.14.2 Dust Grain Formation

Dust grain formation, Figure 3.5, approach is very distinct from the simpler rubble-pile approach. We wanted to simulate the conditions of the environment in which these would form. This included consideration of temperature, which affects particle velocity. At the time of this writing, we have chosen to keep the particle size constant, unlike for rubble piles, as we are still building intuition about the relevant effects of material and environment properties on grain formation. We start with one particle at the origin, and wrote an algorithm which spawns a new particle a safe distance away with its temperature based velocity pointing toward the origin. The particle is then offset perpendicular to its velocity vector within the maximum radius of the existing grain (farthest particle from the origin), and a line-sphere intersection is computed for every particle in the existing cluster with the new particle to verify that a collision will occur and the particle will not be wasted. If no collision will occur, the perpendicular offset is re-rolled and tested until a collision will occur. The simulation is allowed to proceed until the particle collides with and settles on the grain and the process is repeated.

3.15 Rubble-Pile Collision Configurations

Once a set of rubble-piles are formed for the desired experiment, the data for two rubble-piles is read in to the collision simulator. Both have their center of mass computed, and they are positioned along the x axis such that their combined center of mass is at the origin and so that they are not in contact, but very close together

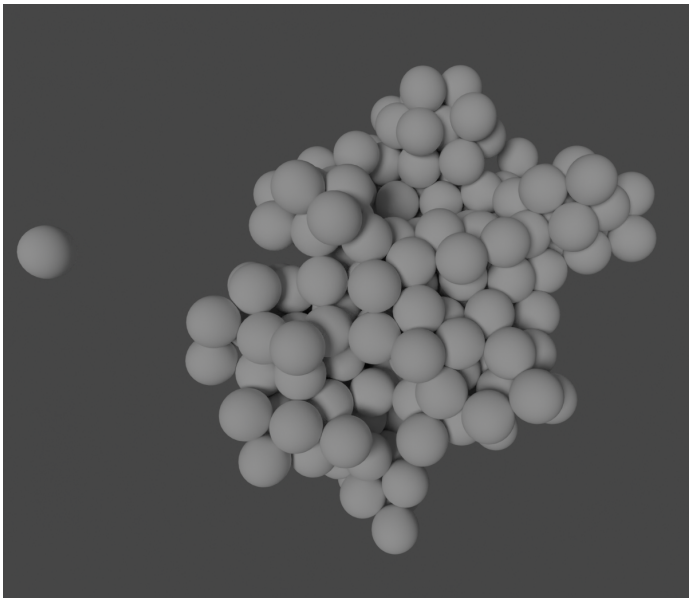

Figure 3.5: A dust grain (right) is formed one particle (left) at a time. The particle on the left is spawned and launched toward the conglomerate grain on the right. Particles are randomly spawned near the grain and launched one at a time to build the grain up.

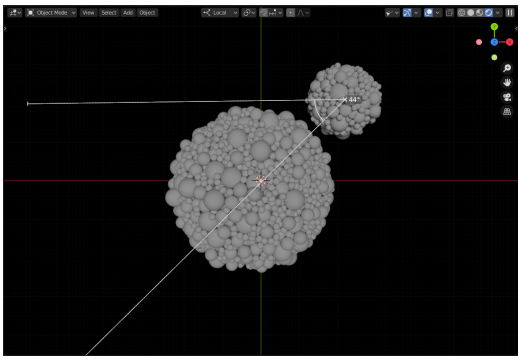

Figure 3.6: Collision configuration for a 44° impact angle in which the mass of the larger cluster is 10 times greater than the mass of the small cluster.

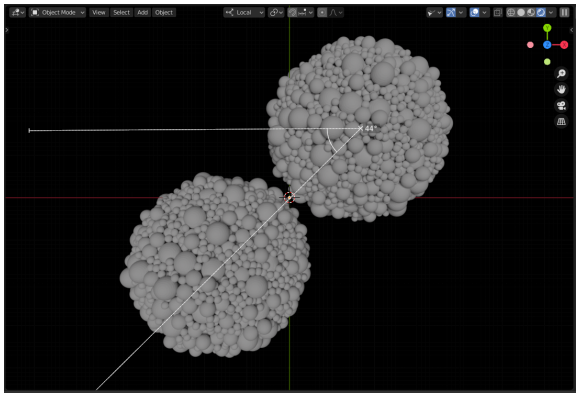

Figure 3.7: Collision configuration for a 44° impact angle in which the masses of the clusters are equal.

Table 3.4: Set of collisions to determine Q^*_{rd}

Particles	Friction	T (as a factor on U)
2560	Yes	1, 3, 4, 5, 6, 6.3, 6.4, 6.55, 7, 8, 10

before the physics simulation begins. The desired collision energy is used to determine the "kick" or velocity applied to all particles in each rubble-pile. This kick is always along the x axis, framed left to right in Figure 3.6. The velocity per rubble-pile is calculated such that the total momentum of the system is zero.

The series of simulations shown in Table 3.4 are performed in a range of collision velocities such that kinetic energy of collision was in the range $1U$ to $10U$, where U is the potential energy of the system including both rubble-piles. The results are analyzed to pinpoint the kinetic energy, T, at which half of the mass of the system remained bound in the largest remnant. This value is conceptually equivalent to Q^*_{RD}, and was found to be approximately $6.4U$ via linear curve fit between the nearest three simulated data points, Figure 3.8.

The potential energy introduced to the system by the starting gap between two rubble-piles was less than 0.001% of total potential energy in all cases.

3.15.1 Spinning Collisions

Collision in which the two rubble-piles have a spin bout the x, y, or z axis are performed for all combinations of positive and negative rotations in all three axis. Table 3.5 shows all combinations simulated. Before simulating the collisions, the previously formed clusters are given an angular velocity by providing a velocity

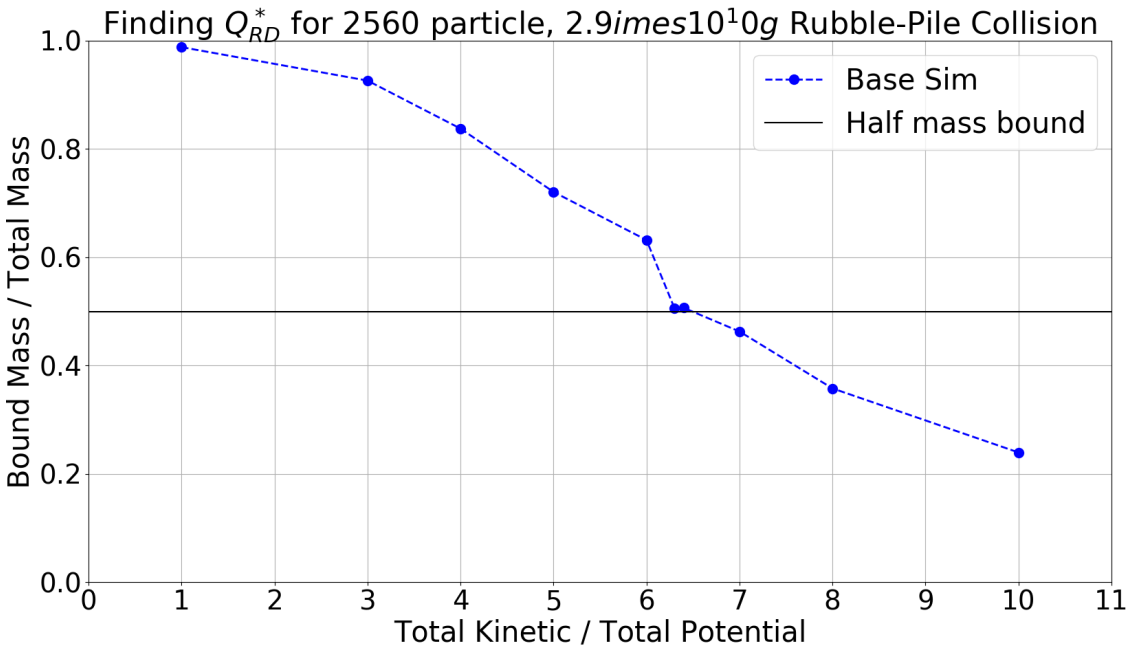

Figure 3.8: Collisions of varied kinetic energy, T, to determine the maximum kinetic energy for maintaining constructive collision (collisions which result in the largest remnant being at least as large as the two initial, identical, rubble-piles)

Table 3.5: A full list of spinning collision combinations simulated. The first two letters in each four letter pair indicate the direction, positive or negative, and and the axis, x, y, or z, for the left cluster as seen in Figure 3.9. The second pair of letters is the same for the right cluster. So, nypx means the left cluster rotates negative about the y axis, and the right cluster rotates positive about the x axis. They are grouped in columns by fundamental spin variations, meaning that pxpx is physically equivalent to nxnx assuming a perfectly uniform spherical cluster. Collision in the same column are expected to have similar collision results.

pxpx	pxnx	pxpy	pypy	pyny	pypz
nxnx	nxpx	pxny	nyny	nypy	pzpy
		pypx	pzpz	pznz	pynz
		nypx	nznz	nzpz	nypz
		pxpz			nynz
		pxnz			nzpy
		pzpx			nzny
		nzpx			pzny
		nxpy			
		nxny			
		pynx			
		nynx			
		nxpz			
		nxnz			
		pznx			
		nznx			

about the center of mass on each particle. The cluster is then allowed to spin for some time to reach the new equilibrium due to its rotation. Note that in Figure 3.9, a spinning cluster gets wider at the equator and narrower pole to pole. Aside from these factors, the process is the same as described for non-spinning collisions.

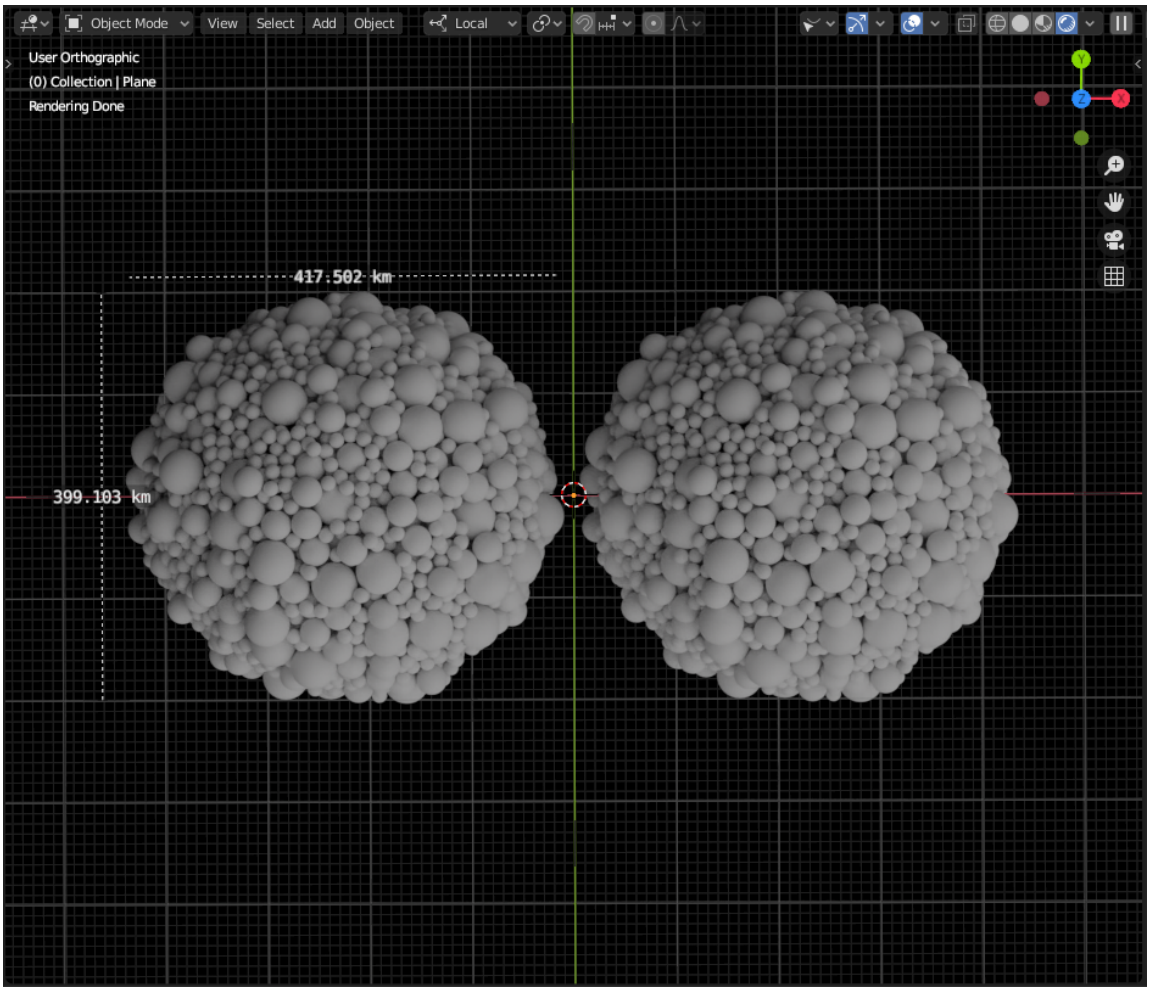

Figure 3.9: Clusters in a spinning collision are first spun up to desired speed and allowed to become stable in their rotation. This results in a squish at the poles and elongation at the equator. In this example, the left cluster has been rotated about a vertical axis at its center of mass, resulting in 417.5 km diameter at its equator, and 399.1 km diameter pole to pole.

Chapter 4: Results

4.1 Significance of Friction

We find that sliding friction plays a significant role in the resilience and energy dissipation of rubble-pile collisions. As seen in Figure 4.1, the bound mass of the largest remnant is greater when sliding friction is enabled. Sliding friction is also critical at the micron scale for maintaining rigid loosely packed dust grains Figure 4.2.

4.2 Literature Comparison

4.2.1 Leinhardt Et al. 2012 Collision Remnant Mass Experiment

Leinhardt Et al. 2012[7] provide a set of simulations for a range of impact parameters (collision offset as opposed to head-on). The results from the reference are compared with a set made to replicate their configurations. Figures 4.3,4.4, and 4.5 show the comparisons.

4.2.2 Sanchez Et al. 2011 Sheet Collapse Experiment

Sanchez Et al. 2011[11] provide an experiement in which a thin sheet of particles is allowed to collapse under its own gravity. A purpose of the experiment is to observe

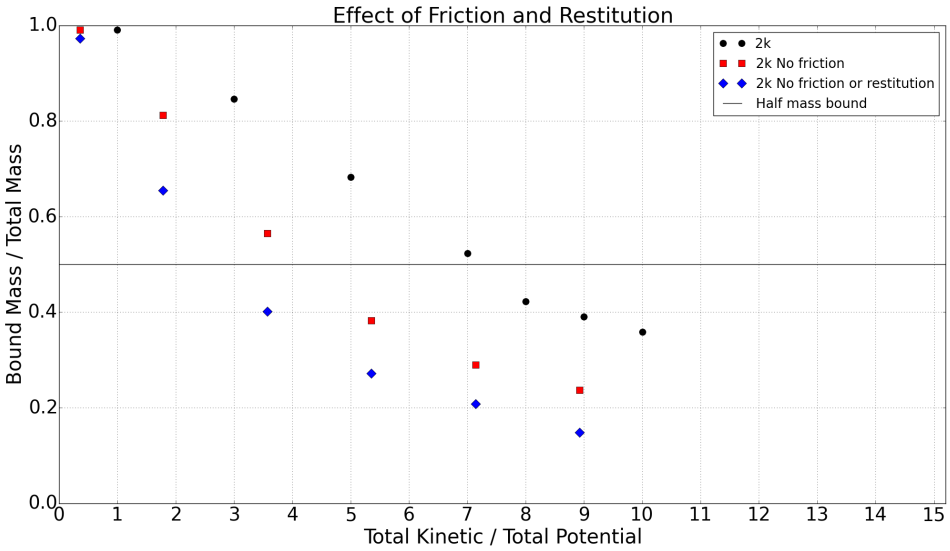

Figure 4.1: Two 2000 particle clusters are collided head on. The bound mass of the largest remnant is greater when sliding friction is enabled (black circle).

the effects of the physics implementation including surface friction, restitution, and gravitational attraction. The resulting shape after collapse is simulated in SpaceLab using the dashpot method described in the literature as well as our own method of restitution.

4.3 Impact Parameter Collisions (Glancing Collision)

A series of glancing collisions are performed to explore the effect of impact parameter on the remnant bound mass after collision. Figure 4.9 shows the results of a series.

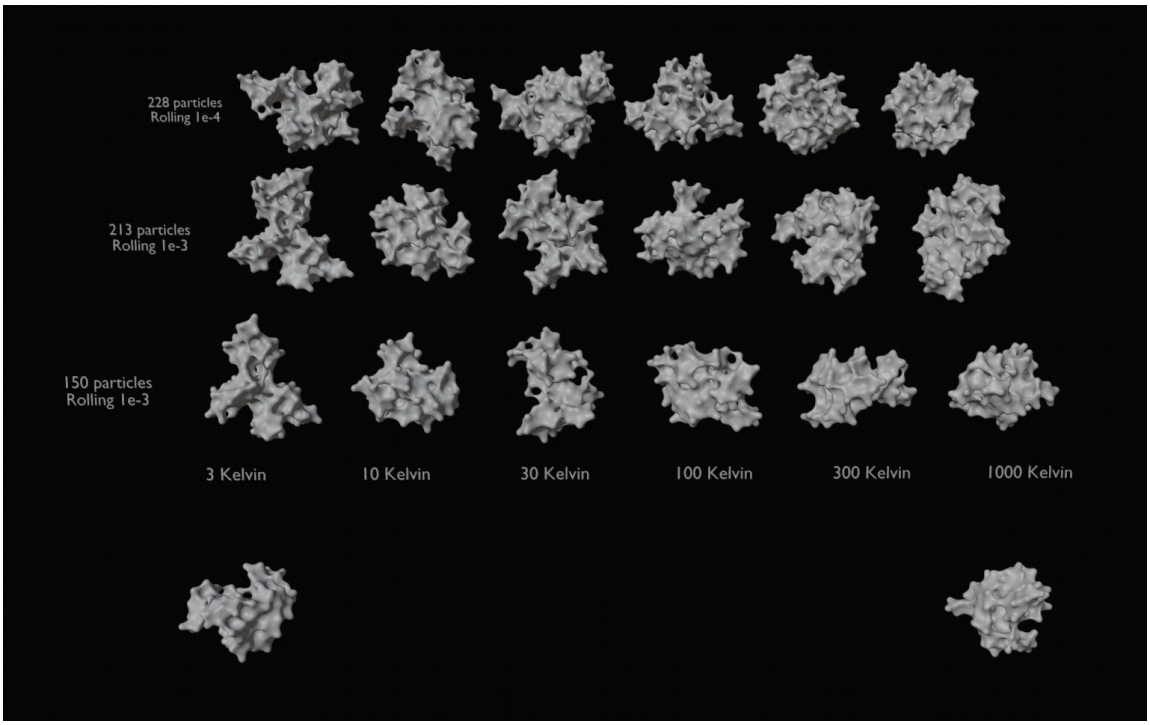

Figure 4.2: Dust grains formed with SpaceLab and visualized with metaballs in Blender.

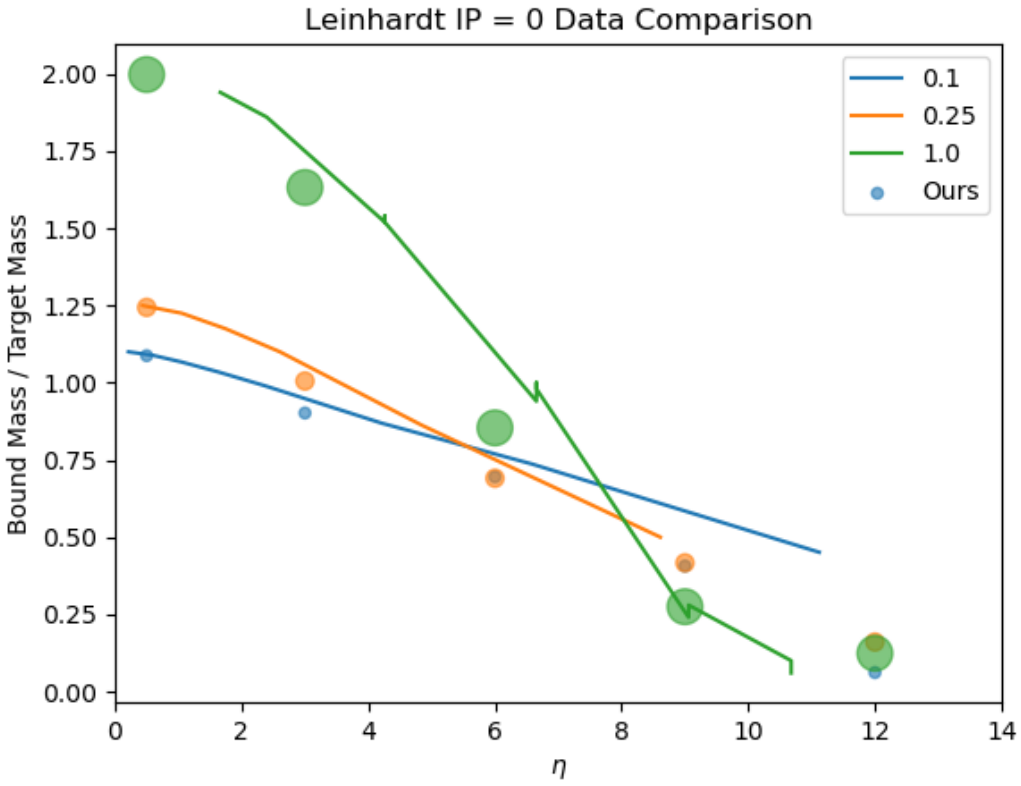

Figure 4.3: Dots represent our results while lines represent results from the literature[7]. The collision carried out here are head-on with and impact parameter of 0. $\eta = \frac{T}{U}$ as defined in section 3.3. 0.1, 0.25, and 1.0 refer to the size ratio between the two rubble-piles. A ratio of 1.0 indicates that the rubble-piles are identical. 0.25 indicates that one rubble pile is $\frac{1}{4}$ of the mass of the other, etc. Refer to Figures 3.6 and 3.7 for collision configuration and diagram of how impact angle is measured.

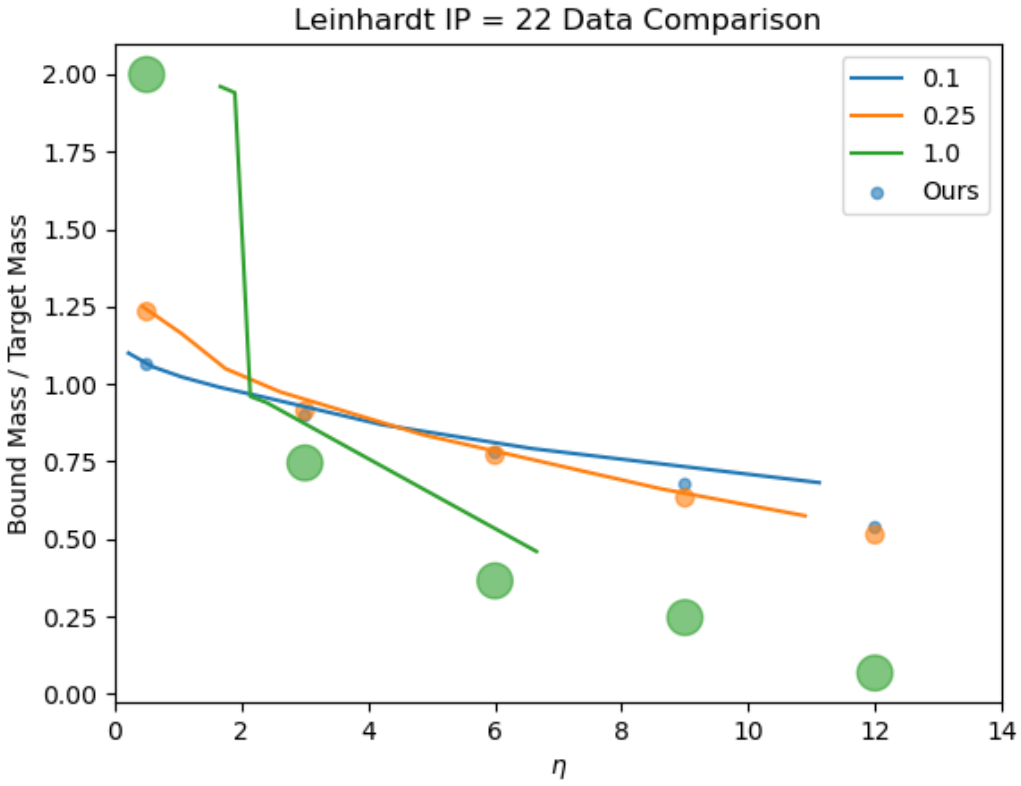

Figure 4.4: Dots represent our results while lines represent results from the literature[7]. The collision carried out here are head-on with and impact angle of 22 degrees. $\eta = \frac{T}{U}$ as defined in section 3.3. 0.1, 0.25, and 1.0 refer to the size ratio between the two rubble-piles. A ratio of 1.0 indicates that the rubble-piles are identical. 0.25 indicates that one rubble pile is $\frac{1}{4}$ of the mass of the other, etc. Refer to Figures 3.6 and 3.7 for collision configuration and diagram of how impact angle is measured.

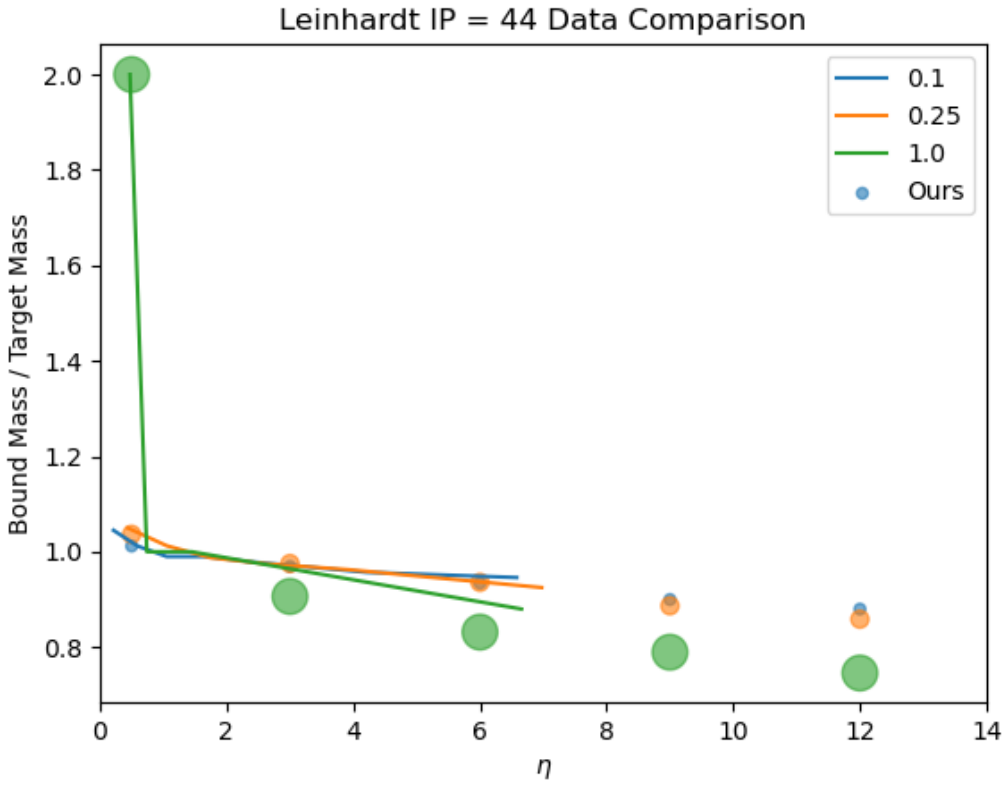

Figure 4.5: Dots represent our results while lines represent results from the literature[7]. The collision carried out here are head-on with and impact angle of 44 degrees. $\eta = \frac{T}{U}$ as defined in section 3.3. 0.1, 0.25, and 1.0 refer to the size ratio between the two rubble-piles. A ratio of 1.0 indicates that the rubble-piles are identical. 0.25 indicates that one rubble pile is $\frac{1}{4}$ of the mass of the other, etc. Refer to Figures 3.6 and 3.7 for collision configuration and diagram of how impact angle is measured.

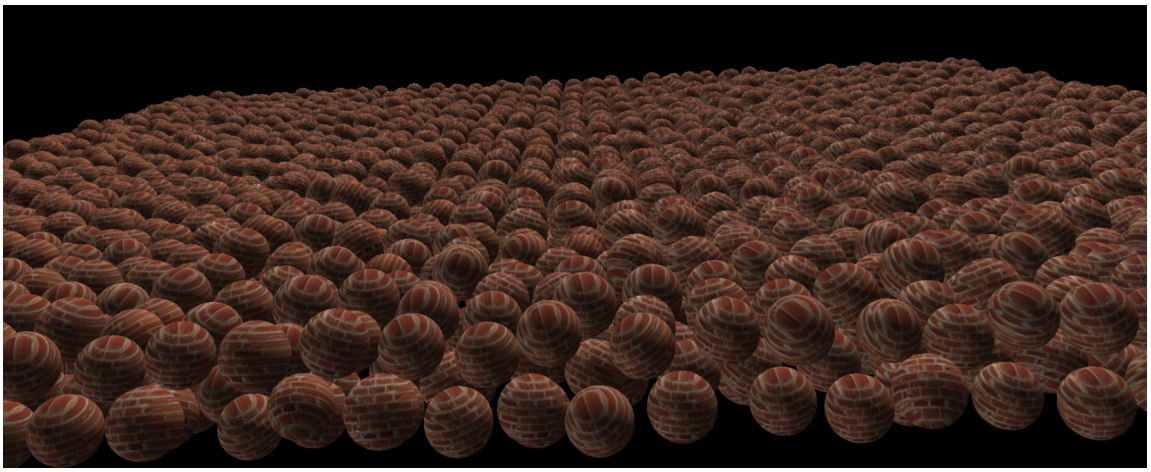

Figure 4.6: A perspective view showing the thickness of the sheet of particles for the comparison with the results of Sanchez Et al.[11].

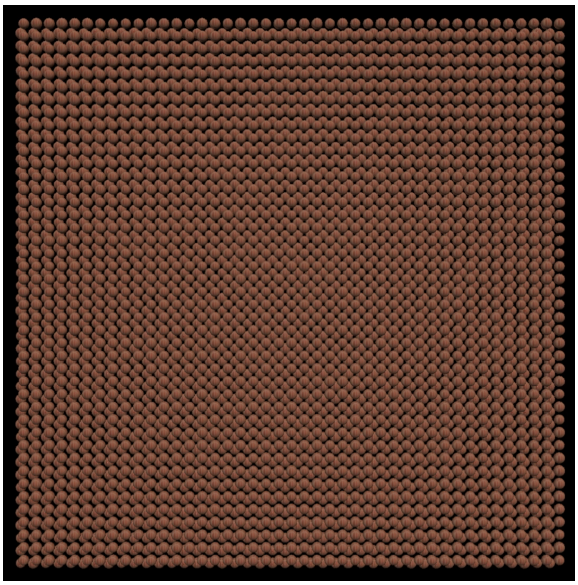

Figure 4.7: Face on view of particle sheet ready to collapse under its own gravity.

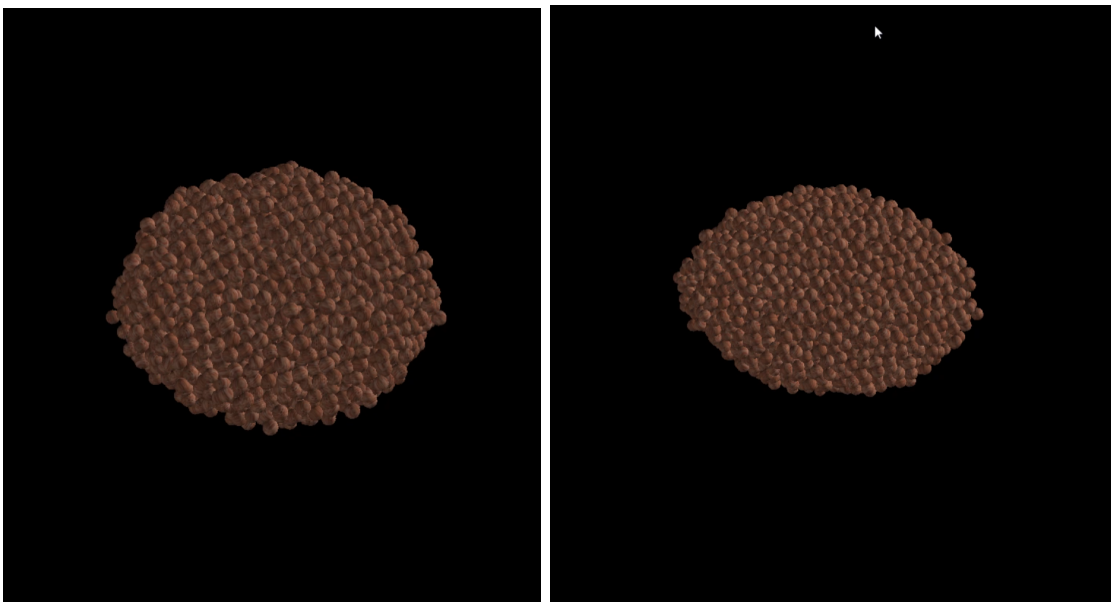

Figure 4.8: Result of our elastic repulsion and restitution method for a sheet of particles collapsing into a lemon shape (left). Result of the dashpot method, Sanchez Et al.[11] for a sheet of particles collapsing into a lemon shape (right).

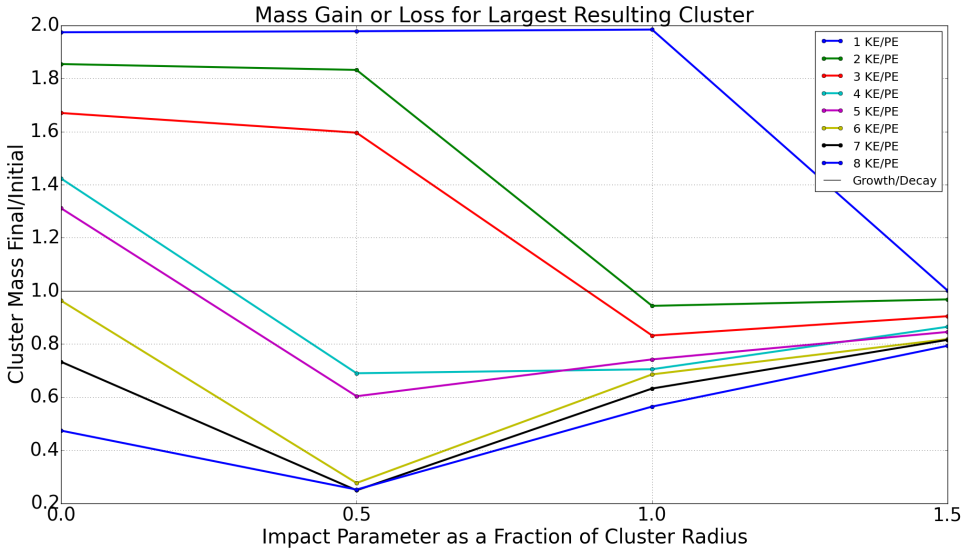

Figure 4.9: Two identical clusters collide off-center. The impact parameter of 1.5 indicates an offset of 1.5 times the radius of a cluster. Intuitively, a more glancing collision typically results in a largest remnant mass close to 1, where 1 is the mass of one of the original clusters. A value of 2 means that the clusters fully merged with no lost particles in collision. However, we do see that there is a turning point somewhere between impact parameter of 0 and 1 in which more mass is lost than in the case of on-center collision. $\frac{KE}{PE}$ is kinetic energy over potential energy equivalent to the previous description of $\eta = \frac{T}{U}$

4.4 Spinning Collisions

Figure 4.12 shows the bound mass to the largest remnant of collision for the 6 fundamental spin combinations from Table 3.5 as well as all combinations at $\eta = 6$ which is near the energy at which the collision results in a remnant equal to the size of one of the original clusters. Figures 4.11 and 4.10 show two examples mid collision of the range of complexity in spinning interactions. Figure 4.11 is intuitively symmetric, where as Figure 4.10 is quite complex and chaotic. Animated reference is available at https://sss.aeromap.org/animations.

4.5 Collision Remnant Identification

Collision remnant identification provides valuable insight into how matter from an asteroid is shared with another. Figure 4.13 shows the pre-collision coloring of what will be the 5 largest bound remnants. Figure 4.14 shows how they are distributed as they drift apart, unbound from each other.

4.6 Dynamic Time and the DART Mission Simulation

When velocity based dynamic time-step size was implemented for the very high velocity of the DART probe impact with the moonlet Didymos b, the energy conservation difference between a static and dynamic time-step was assessed to be sure that dynamic time step would not significantly impact results. At very low velocities, the dynamic time-step size goes above the static $0.04s$. At that point the accuracy of

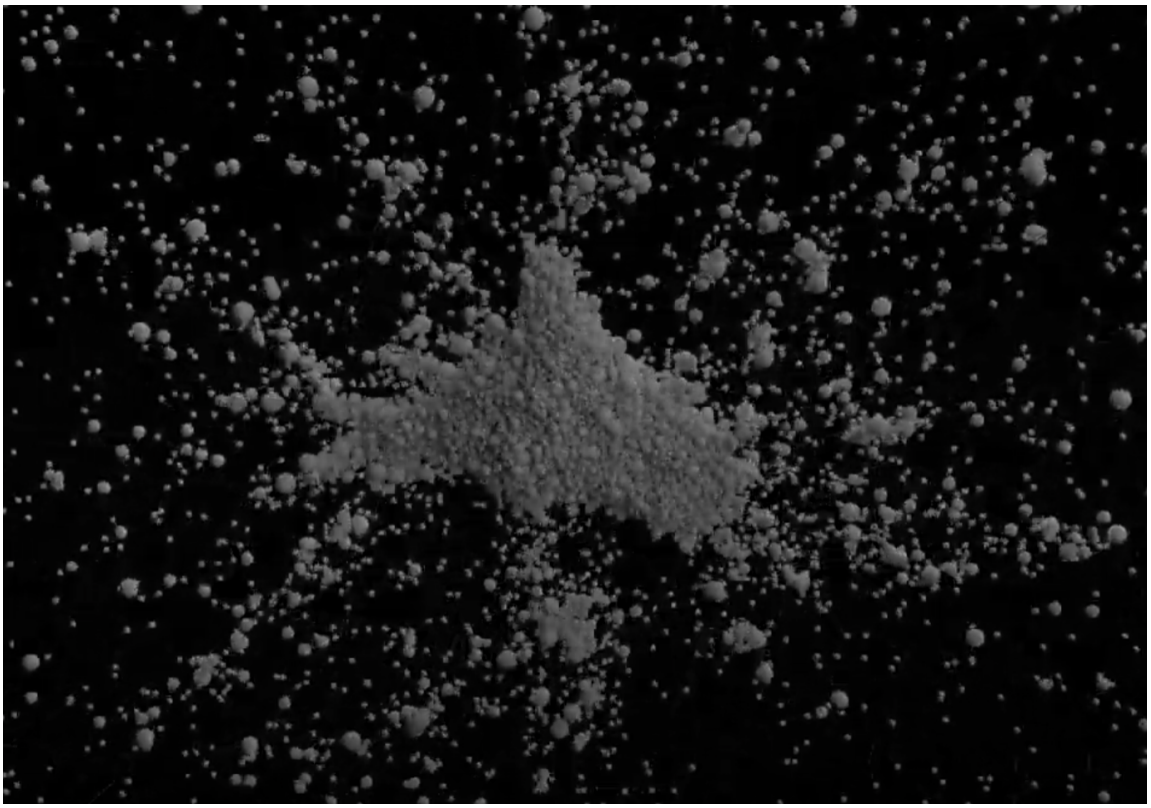

Figure 4.10: Mid collision complexity shown when one cluster is rotating positive on the x axis, while the other is rotating positive on the z axis. Animation available at https://sss.aeromap.org/animations

Figure 4.11: Mid collision symmetry in positive y vs positive y rotation. Animation available at https://sss.aeromap.org/animations

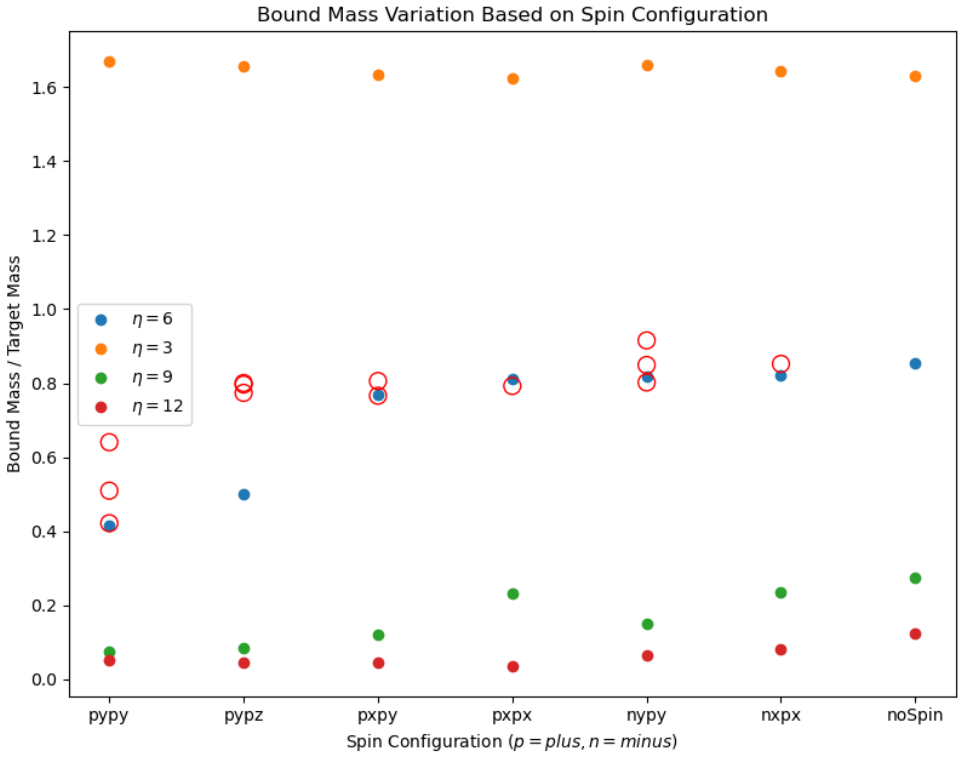

Figure 4.12: Two identical rubble-pile clusters are collided with combinations of spins indicated for example by $nxpx$. where the left cluster is spinning around the x axis in the, n, negative direction, and the right cluster is spinning around the x axis in the positive direction. All collisions in this plot occur along the x axis. η indicates the energy of collision. $\eta = T/U$. Note that target mass here is the mass of one of the two identical clusters, there for a completely constructive collision results in a Bound Mass / Target mass of 2.0. All collision remnants below 1.0 are destructive.

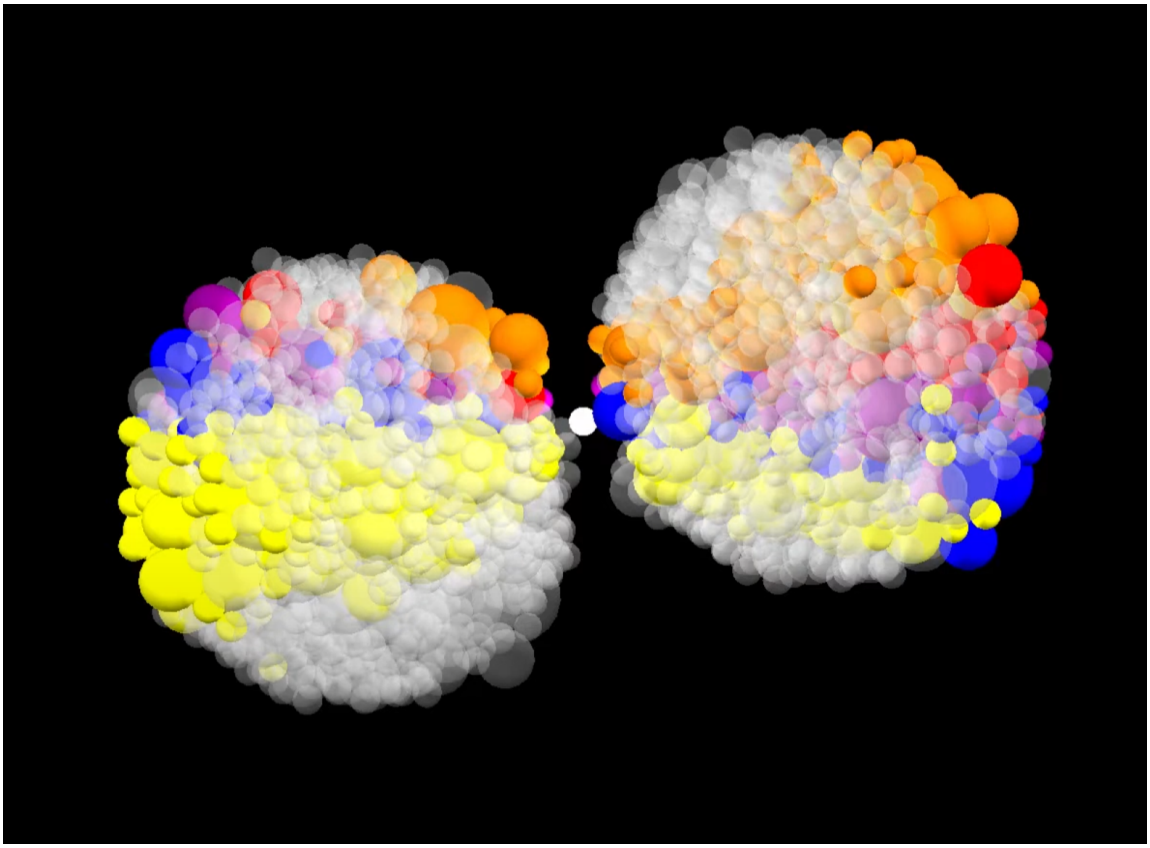

Figure 4.13: A collision is post-processed to determine groups of gravitationally bound particles. They are colored for each remnant. Here the 5 largest remnants of collision are visualized in solid colors. The semi-transparent particles are not bound to any of the 5 identified remnants.

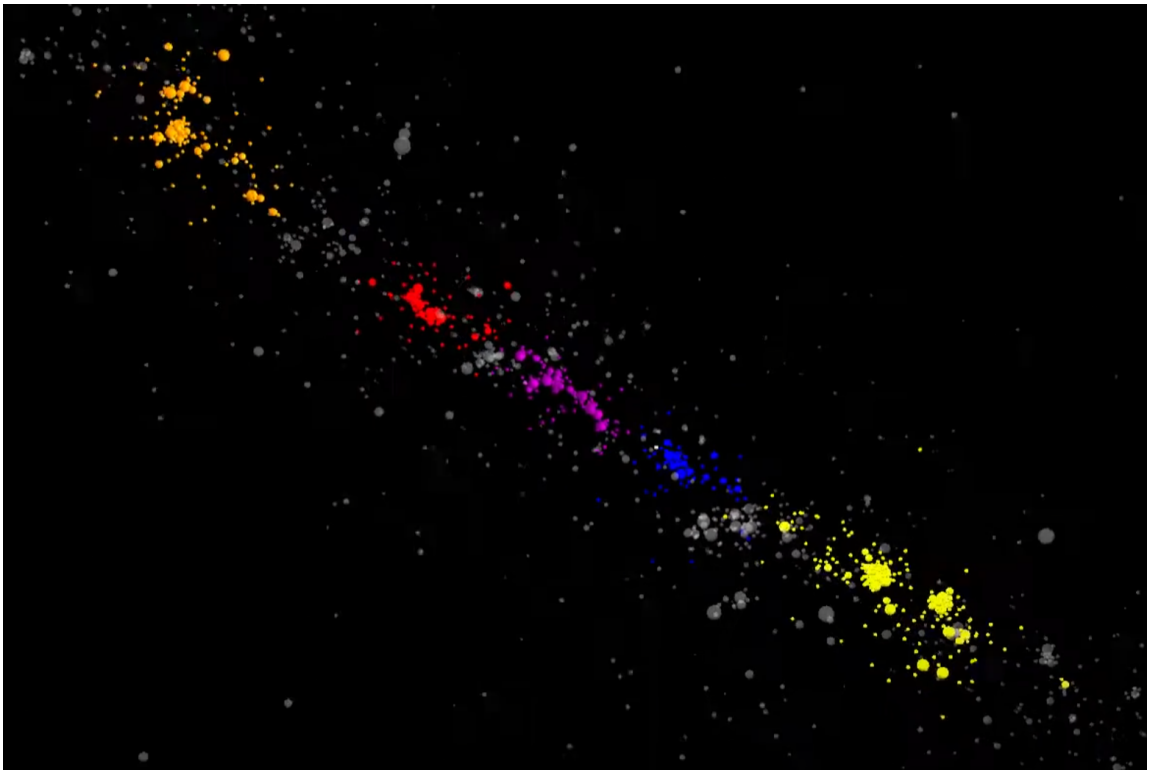

Figure 4.14: This is the post-collision state at which the bound remnants are identified. The group colors are consistent between this figure and Figure 4.13.

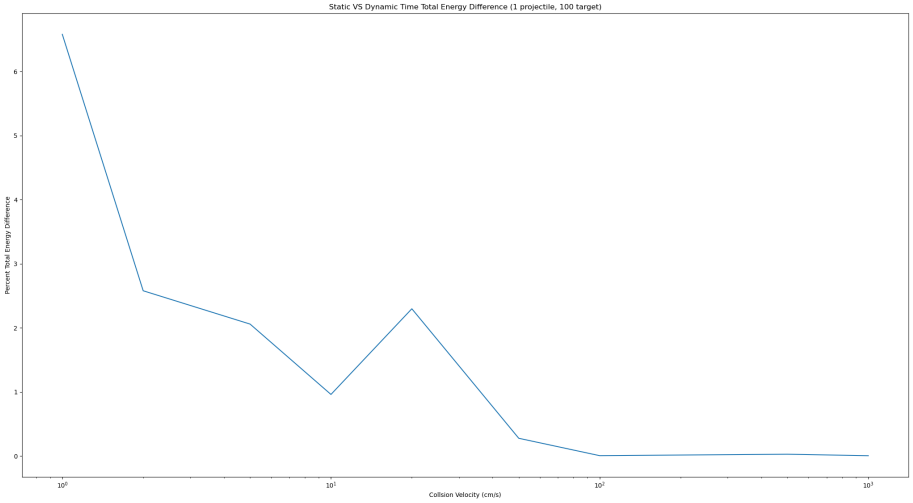

Figure 4.15: Several simulations are carried out with a single particle projectile impacting a 100 particle target cluster at increasing velocities. The difference between the static and dynamic time step total energy after collision is shown and converges at higher velocities.

total energy degrades. The DART probe begins at 6km/s on impact, and for the entirety of the DART simulation, the particle velocity maximum kept the time-step below $0.04s$. Particles ejected far from the moonlet or on a velocity vector away from the surface are not considered for the dynamic time-step calculation to allow the simulation to speed up more quickly. Figure 4.15 shows the comparison between dynamic and static time-step.

Chapter 5: Summary and Conclusions

5.1 Future Publications

5.1.1 Rubble-Pile Asteroid Collision Remnant Growth Constraints

This will be our first paper and the research and results are complete. This paper will explore in better detail the full gambit of rubble-pile asteroid simulations performed, proof of SpaceLab result validity via literature comparison, and constraints for remnant growth under a set of material and environmental conditions based on current knowledge of asteroid composition.

5.1.2 DART Aftermath Simulation

This exciting mission launched in November of 2021 and is planned to impact its target moonlet late in 2022. We intend to publish our prediction of the impact result. Figures 5.1 and 5.2 provide a preview of the simulation results from two angles and different times in the simulation.

5.1.3 Dust Conglomeration and Resilience in the Early Solar System

This work will fulfill the requirements of NASA grants 80NSSC18K1729 and uses SpaceLab in its most recent and advanced state. The additions of VDW force and

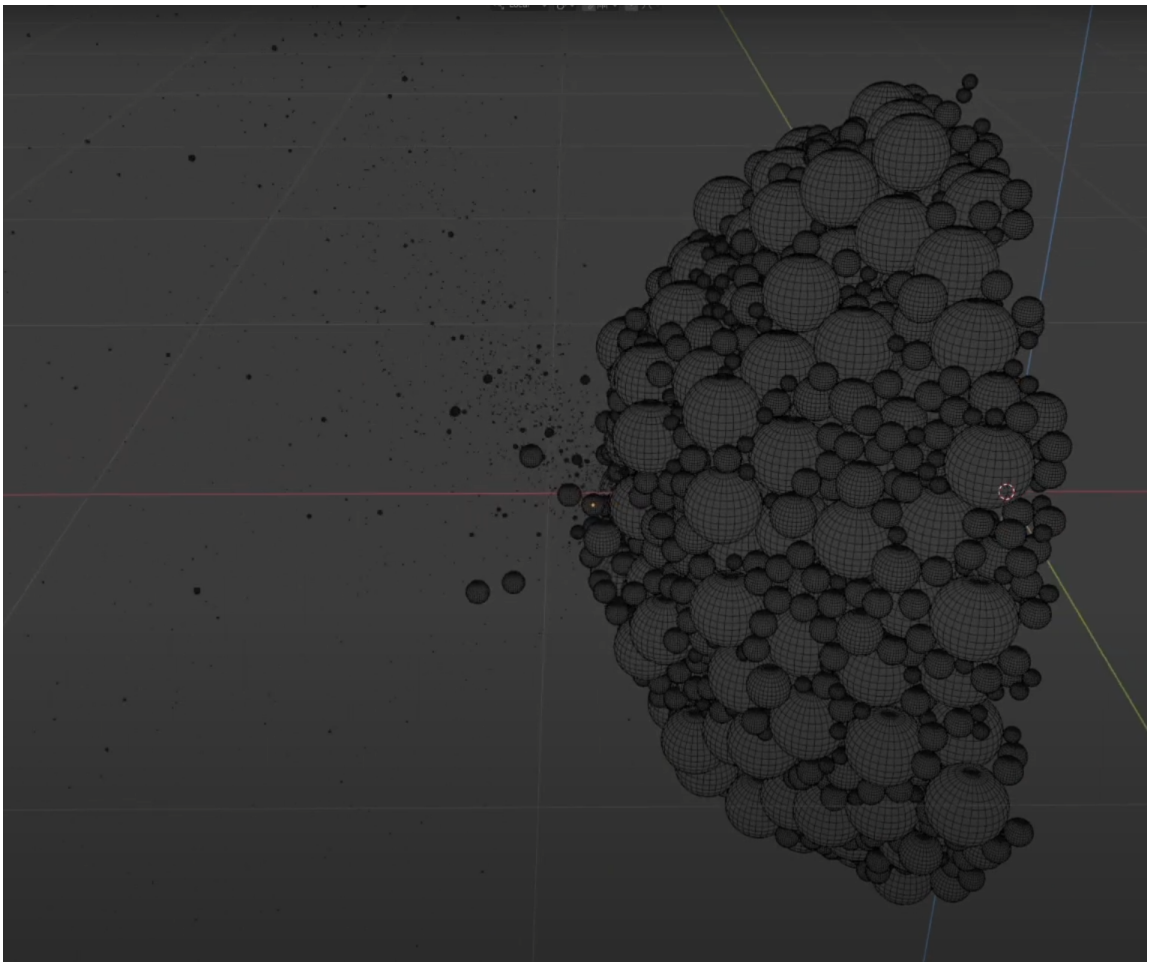

Figure 5.1: Simulation of probe impact with moonlet. NASA's DART mission currently in progress

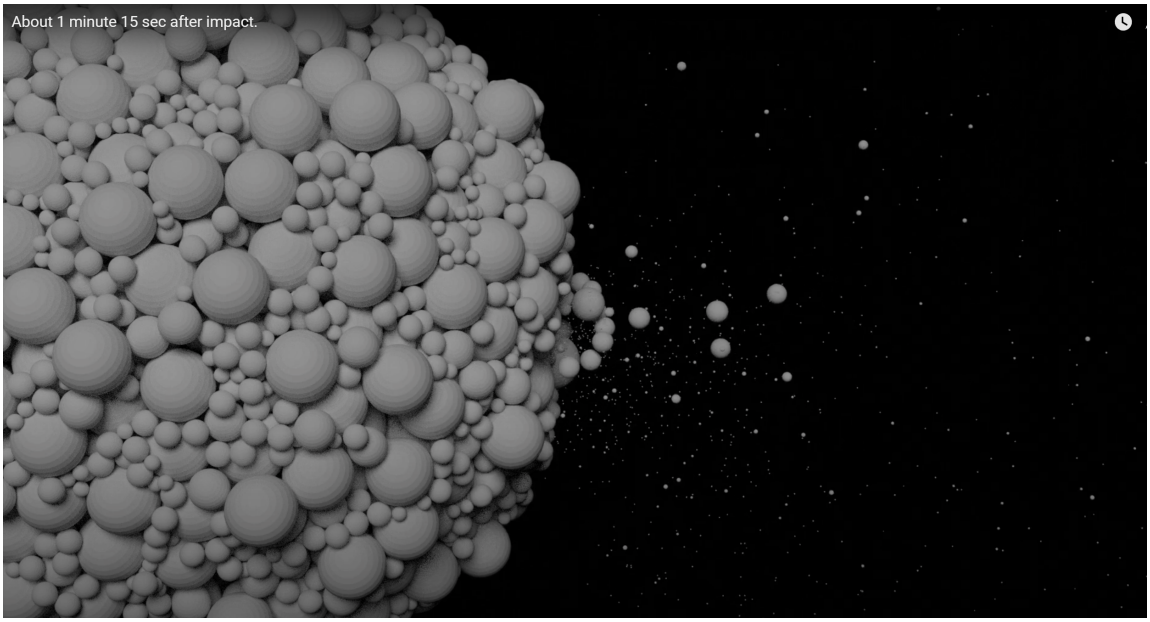

Figure 5.2: 75 seconds after probe impact on moonlet.

rolling friction opens the way to exciting new discoveries and intuition of micron scale forces and dust conglomeration.

5.2 Future SpaceLab Improvements

The next goal for SpaceLab is to make use of what I have learned in my short time in the visual effect industry to vastly improve the performance and usability of the software. Work has begun on the use of a Barnes-Hut tree to reduce the number of computations per time-step, improvements to adaptive times-stepping, and the use of the OpenVDB file format compatible with state of the art visualization software. Once a tree structure is implemented, we will also be able to make more extensive use of parallelism and MPI. These changes will allow for higher resolution simulations.

A user interface is also being considered among other quality of life improvements.

5.3 Valuable Lessons Learned

The single biggest mistake made and lesson learned through this research has been a failure to maintain a timeline of data, and corresponding documentation of work. Early in the project I attempted to keep notes of updates to the software, explanations of choices, and detailed documentation of experiments and the subtle challenges along the way, but more often than not, that information was not well kept, resulting in inconsistent figure production, and hard work not accounted for or on display. This experience will stay with me deep into my career, and though organizing and documenting well is still a great challenge, it is one to be taken extremely seriously. It is also one for which I am finding the value is in the process as much as the later reference.

Bibliography

[1] Nasa asteroids missions,
https://nssdc.gsfc.nasa.gov/planetary/planets/asteroidpage.html.

[2] Edward Beshore, Dante Lauretta, William Boynton, Christopher Shinohara, Brian Sutter, David Everett, Jonathan Gal-Edd, Ronald Mink, Michael Moreau, and Jason Dworkin. The osiris-rex asteroid sample return mission. In *2015 IEEE Aerospace Conference, AERO 2015*, IEEE Aerospace Conference Proceedings. IEEE Computer Society, June 2015. Publisher Copyright: © 2015 IEEE.; 2015 IEEE Aerospace Conference, AERO 2015 ; Conference date: 07-03-2015 Through 14-03-2015.

[3] Andrew F. Cheng, Andrew S. Rivkin, Patrick Michel, Justin Atchison, Olivier Barnouin, Lance Benner, Nancy L. Chabot, Carolyn Ernst, Eugene G. Fahnestock, Michael Kueppers, Petr Pravec, Emma Rainey, Derek C. Richardson, Angela M. Stickle, and Cristina Thomas. Aida dart asteroid deflection test: Planetary defense and science objectives. *Planetary and Space Science*, 157:104–115, 2018.

[4] G.J. Flynn, L.B. Moore, and W. Klöck. Density and porosity of stone meteorites: Implications for the density, porosity, cratering, and collisional disruption of asteroids. *Icarus*, 142(1):97–105, 1999.

[5] B. Imre, S. Räbsamen, and Sarah Springman. A coefficient of restitution of rock materials. *Computers & Geosciences*, 34:339–350, 04 2008.

[6] Shota Kikuchi, Takanao Saiki, Yuto Takei, Fuyuto Terui, Naoko Ogawa, Yuya Mimasu, Go Ono, Kent Yoshikawa, Hirotaka Sawada, Hiroshi Takeuchi, Hitoshi Ikeda, Atsushi Fujii, Seiji Sugita, Tomokatsu Morota, Manabu Yamada, Rie Honda, Yasuhiro Yokota, Naoya Sakatani, Shingo Kameda, Toru Kouyama, Naru Hirata, Naoyuki Hirata, Kei Shirai, Kohei Kitazato, Satoru Nakazawa, Makoto Yoshikawa, Satoshi Tanaka, Koji Wada, Sei ichiro Watanabe, and Yuichi Tsuda. Hayabusa2 pinpoint touchdown near the artificial crater on ryugu: Trajectory design and guidance performance. *Advances in Space Research*, 68(8):3093–3140, 2021.

[7] Zoë M. Leinhardt and Sarah T. Stewart. Collisions between Gravity-dominated Bodies. I. Outcome Regimes and Scaling Laws. *apj*, 745(1):79, January 2012.

[8] Zoë M. Leinhardt and Sarah T. Stewart. COLLISIONS BETWEEN GRAVITY-DOMINATED BODIES. i. OUTCOME REGIMES AND SCALING LAWS. *The Astrophysical Journal*, 745(1):79, dec 2011.

[9] Piotr Małkowski, Łukasz Ostrowski, and Jarosław Brodny. Analysis of young's modulus for carboniferous sedimentary rocks and its relationship with uniaxial compressive strength using different methods of modulus determination. *Journal of Sustainable Mining*, 17(3):145–157, 2018.

[10] Susanne Pfalzner and Paul Gibbon. *Many-Body Tree Methods in Physics*. Cambridge University Press, 1996.

[11] Paul Sánchez and Daniel J. Scheeres. SIMULATING ASTEROID RUBBLE PILES WITH a SELF-GRAVITATING SOFT-SPHERE DISTINCT ELEMENT METHOD MODEL. *The Astrophysical Journal*, 727(2):120, jan 2011.

[12] A. P. Santos, Dan S. Bolintineanu, Gary S. Grest, Jeremy B. Lechman, Steven J. Plimpton, Ishan Srivastava, and Leonardo E. Silbert. Granular packings with sliding, rolling, and twisting friction. *Phys. Rev. E*, 102:032903, Sep 2020.

[13] Raihan Tayeb, Xin Dou, Yijin Mao, and Yuwen Zhang. Analysis of cohesive microsized particle packing structure using history-dependent contact models. *Journal of Manufacturing Science and Engineering*, 138(4), oct 2015.

[14] Colin Thornton. *Granular dynamics, contact mechanics and particle system simulations: A dem study*. SPRINGER INTERNATIONAL PU, 2016.

[15] Loup Verlet. Computer "experiments" on classical fluids. i. thermodynamical properties of lennard-jones molecules. *Phys. Rev.*, 159:98–103, Jul 1967.

APPENDICES

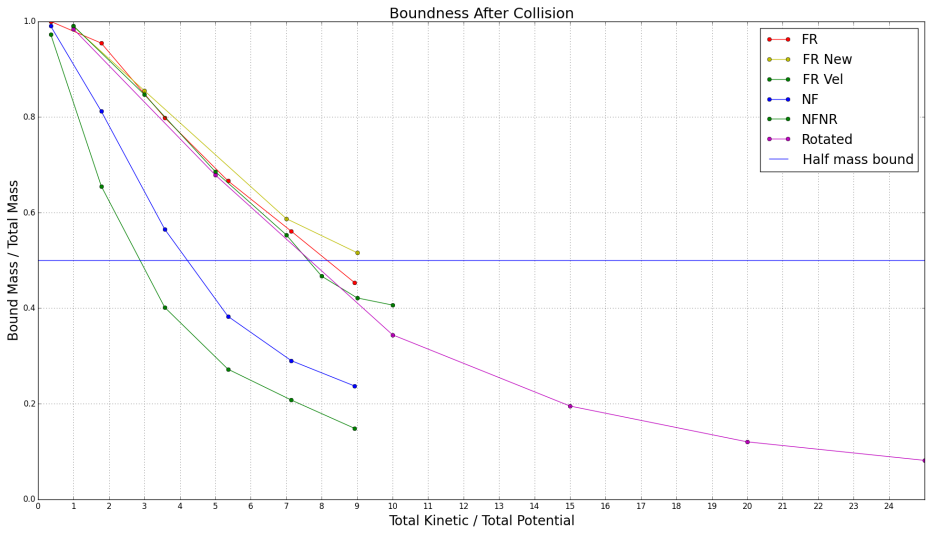

Figure 3: Bound mass after collision

The code for SpaceLab is available upon request to the author. It is currently not publicly listed on github for reasons related to my employment.

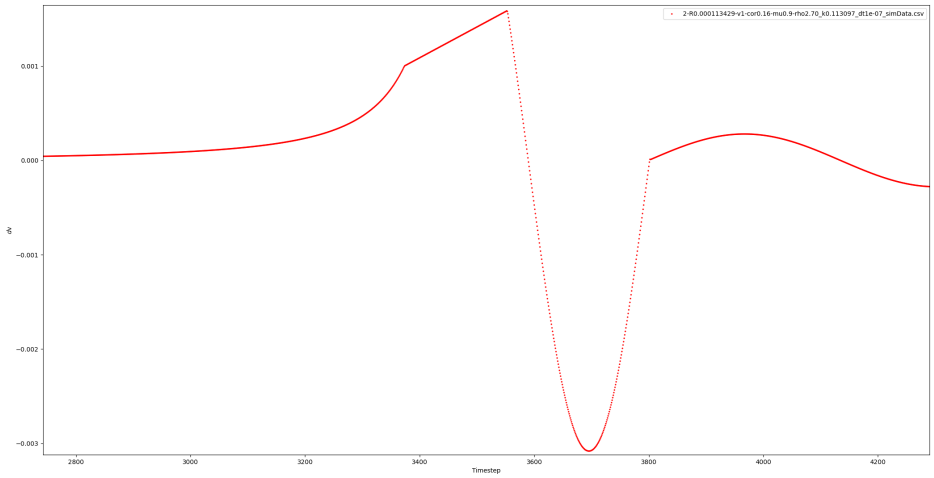

Figure 4: Van Der Waals force implementation verification. Velocity of a particle in a particle pair interaction is expected to increase exponentially according to (3.13) until a specified minimum distance, at which point the distance h is considered constant. This is necessary to protect against instability due to the extremely exponential nature of VDW force.

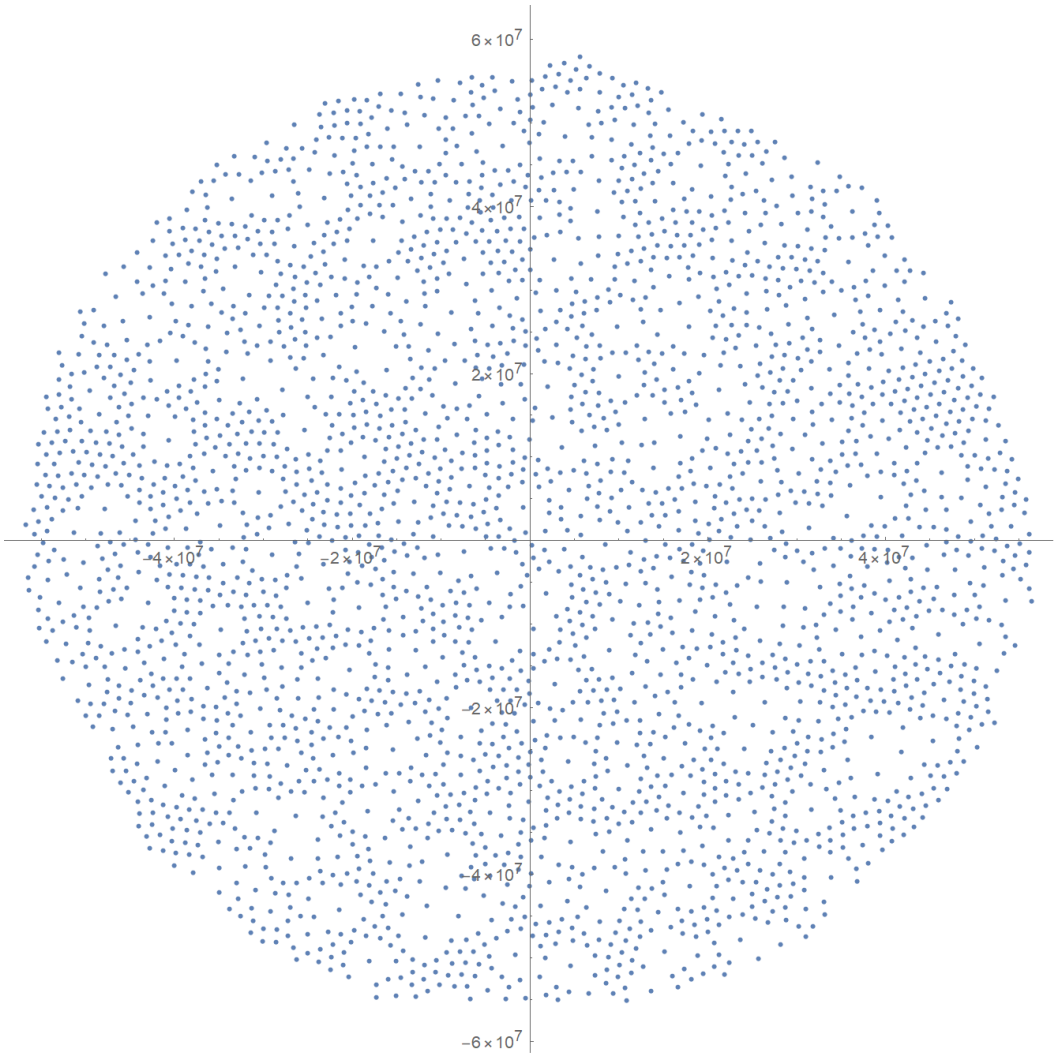

Figure 5: 2D experiment showing the stress chain phenomena in SpaceLab. Point plot before collapse.

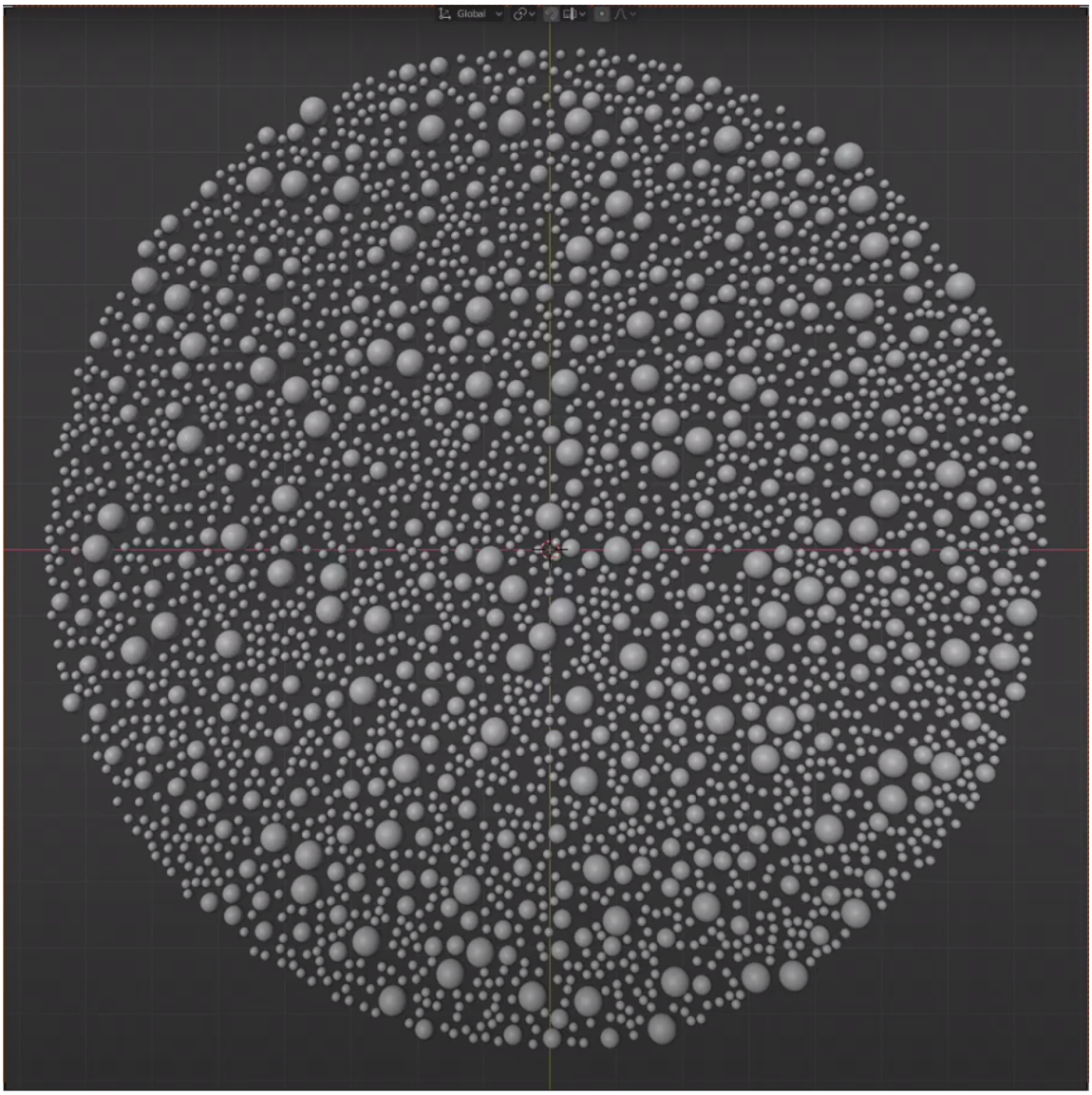

Figure 6: 2D experiment showing the stress chain phenomena in SpaceLab. 3D Particle representation before collapse.

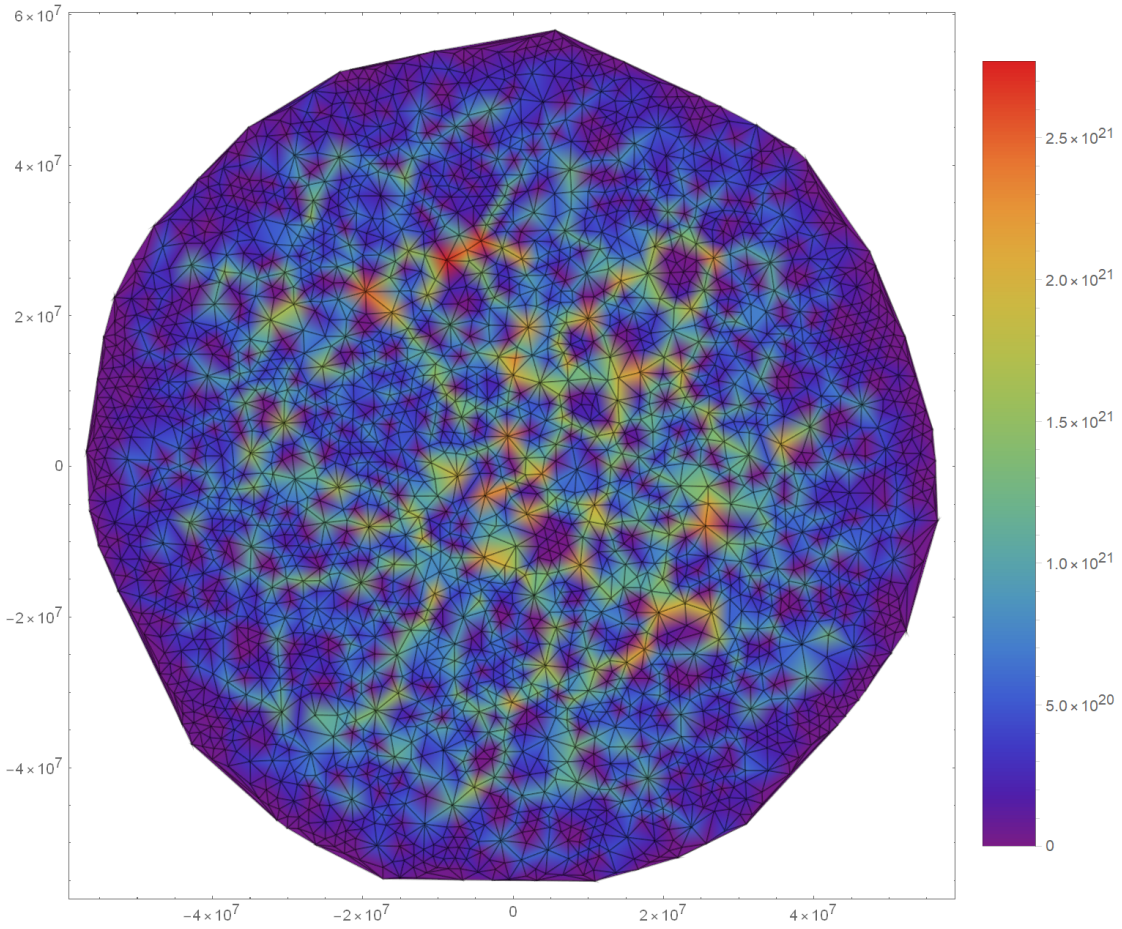

Figure 7: 2D experiment showing the stress chain phenomena in SpaceLab. Delaunay triangulation and heatmap of particle compression to identify stress chains.

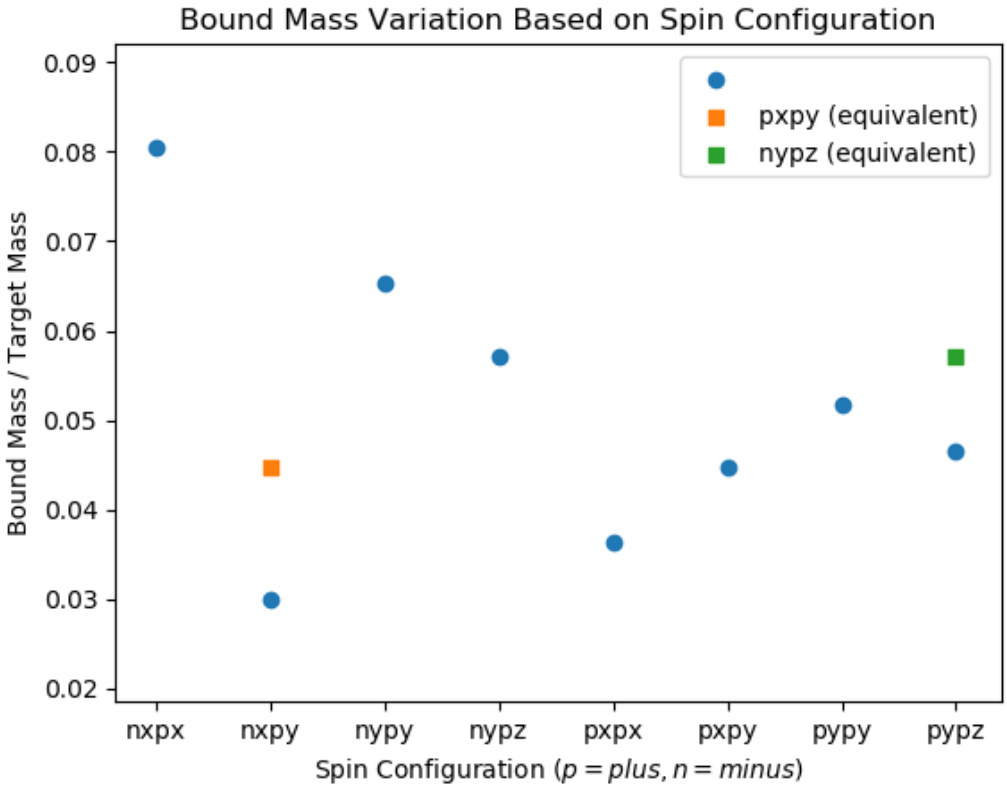

Figure 8: High speed collisions, $\eta = 12$, variation in bound mass per spin configuration.

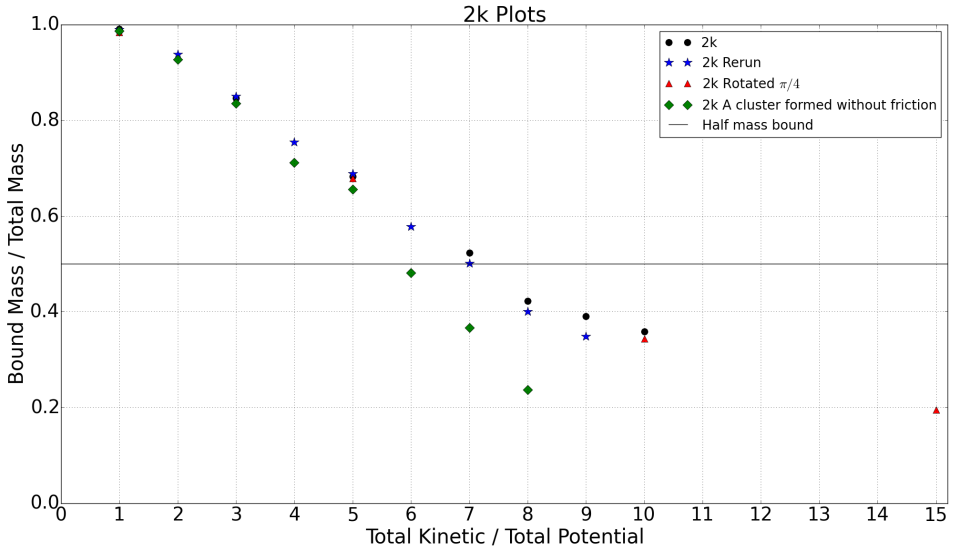

Figure 9: Test on cube shaped cluster collisions comparing face collisions to edge collision.